Ti-poor high-Al chromitites of the Moa-Baracoa ophiolitic massif (eastern Cuba) formed in a nascent forearc mantle

Hui-Chao Rui [a], Jing-Sui Yang [b,c,*], Angélica I. Llanes Castro [d], Jian-Ping Zheng [a], Dong-Yang Lian [b], Wei-Wei Wu [b], Yurisley Valdes Mariño [e]

[a] *School of Earth Sciences, China University of Geosciences, Wuhan 430074, China*
[b] *School of Earth Sciences and Engineering, Nanjing University, Nanjing 210023, China*
[c] *Center for Advanced Research on the Mantle (CARMA), Chinese Academy of Geological Sciences, Beijing 100037, China*
[d] *Department of Petrology and Mineralogy, Institute of Geology and Paleontology, Havana 10200, Cuba*
[e] *High Mining Metallurgic Institute of Moa "Dr. Antonio Nunez Jimenez", Moa 83310, Cuba*

ARTICLE INFO

ABSTRACT

Podiform chromitite is an important archive recording detailed information on mantle magmatism, heterogeneity and dynamics. High-Al chromitites are believed to have formed in mid-ocean ridge, back-arc, and forearc basin environments. Correlation between the geochemical composition of high-Al chromitites and their geodynamic settings is not well explored. Here, we present the petrographic, microstructural, mineral chemical, and whole-rock platinum-group element (PGE) data of the high-Al podiform chromitites from the Moa-Baracoa ophiolitic massif (MBOM) (eastern Cuba), to investigate their petrogenesis and constrain their geodynamic settings. The chromitites occur in massive and semi-massive forms enveloped in dunite within the host harzburgite. The Cr-spinels in these chromitites contain inclusions of silicates (e.g., clinopyroxene, amphibole, and phlogopite), platinum-group minerals, and base-metal sulfides. These chromitites (Cr# = 42.5–54.7, Mg# = 64.1–75.5) are poor in TiO_2 (0.02–0.15 wt%), and display an obvious enrichment in IPGE (Os, Ir, and Ru) over PPGE (Rh, Pt, and Pd). Cr-spinel grains usually show low-pressure characteristics illustrated by inclusions of amphibole and phlogopite. Additionally, high-pressure/high-temperature microstructures, such as densely exsolved needles of clinopyroxene, strong crystal-plastic deformation, and overgrowth, can be found in some Cr-spinels. The coexistence of high- and low-pressure characteristics implies that some Cr-spinel grains crystallized in a relatively deep mantle while others crystallized at a shallow depth. Mineralogical and chemical features indicate that the parental magma of the chromitites was hydrous and TiO_2-poor, and had high oxygen fugacity. We propose that the Ti-poor high-Al chromitite of the MBOM originated from a nascent forearc mantle during subduction initiation, in which deep-crystallized Cr-spinel were carried upward by the parental melt and deposited together with the shallow-crystallized crystals.

1. Introduction

Podiform chromite deposits have been widely reported in Phanerozoic ophiolites (e.g., Arai and Ahmed, 2018; Arai and Miura, 2016; Augé, 1987; Rollinson and Adetunji, 2013; Saveliev, 2021; Wu et al., 2021; Xiong et al., 2015; Yang et al., 2015, 2021; Zhou et al., 2014; Zhu and Zhu, 2020), and are known to provide detailed information on various magmatic processes (Chen et al., 2021; González-Jiménez et al., 2014; Su et al., 2016; Uysal et al., 2018; Xiong et al., 2017a; Zhou et al., 1994, 2014), mantle heterogeneity (Frei et al., 2006; Shi et al., 2007),

and mantle dynamics (Arai, 2013; Yang et al., 2021). However, the origin of podiform chromite deposits is still not completely understood. The most prevalent petrogenetic model of chromitites is melt-peridotite interactions and subsequent mingling and/or mixing of variably evolved melts in the shallow mantle led to Cr saturation and Cr-spinel precipitation in the conduits of a dynamic magma system (Arai and Miura, 2016; González-Jiménez et al., 2014; Zhou et al., 1996, 2014). Matveev and Ballhaus (2002) and Su et al. (2020) highlighted the contribution of fluid immiscibility to Cr-spinel crystallization.

Based on the Cr# [$100 \times Cr/(Cr + Al)$] values of Cr-spinel,

---

chromitites are classified as: high-Cr (Cr# >60) and high-Al (Cr# <60) (e.g., Arai and Ahmed, 2018; Rollinson, 2008; Zhou et al., 2014). Additionally, Uysal et al. (2018) distinguished intermediate varieties (Cr# = 50–70). The geochemical composition of chromitites is indicative of their parental melts. For example, high-Cr chromitites are interpreted to have precipitated from boninitic melts, whereas high-Al chromitites are believed to have crystallized from mid-oceanic ridge

basalt (MORB)-like tholeiitic magmas (Kamenetsky et al., 2001; Zhou et al., 2014). Generally, high-Al chromitites have relatively higher contents of TiO_2 than the high-Cr varieties (e.g., Pagé and Barnes, 2009; Zhou et al., 2014; Zhu and Zhu, 2020) because of their higher content in MORBs as compared to in boninites (e.g., Pagé and Barnes, 2009, and references therein). However, a few high-Al chromitites with very low contents of TiO_2 have also been reported in previous works (e.g., Xiong
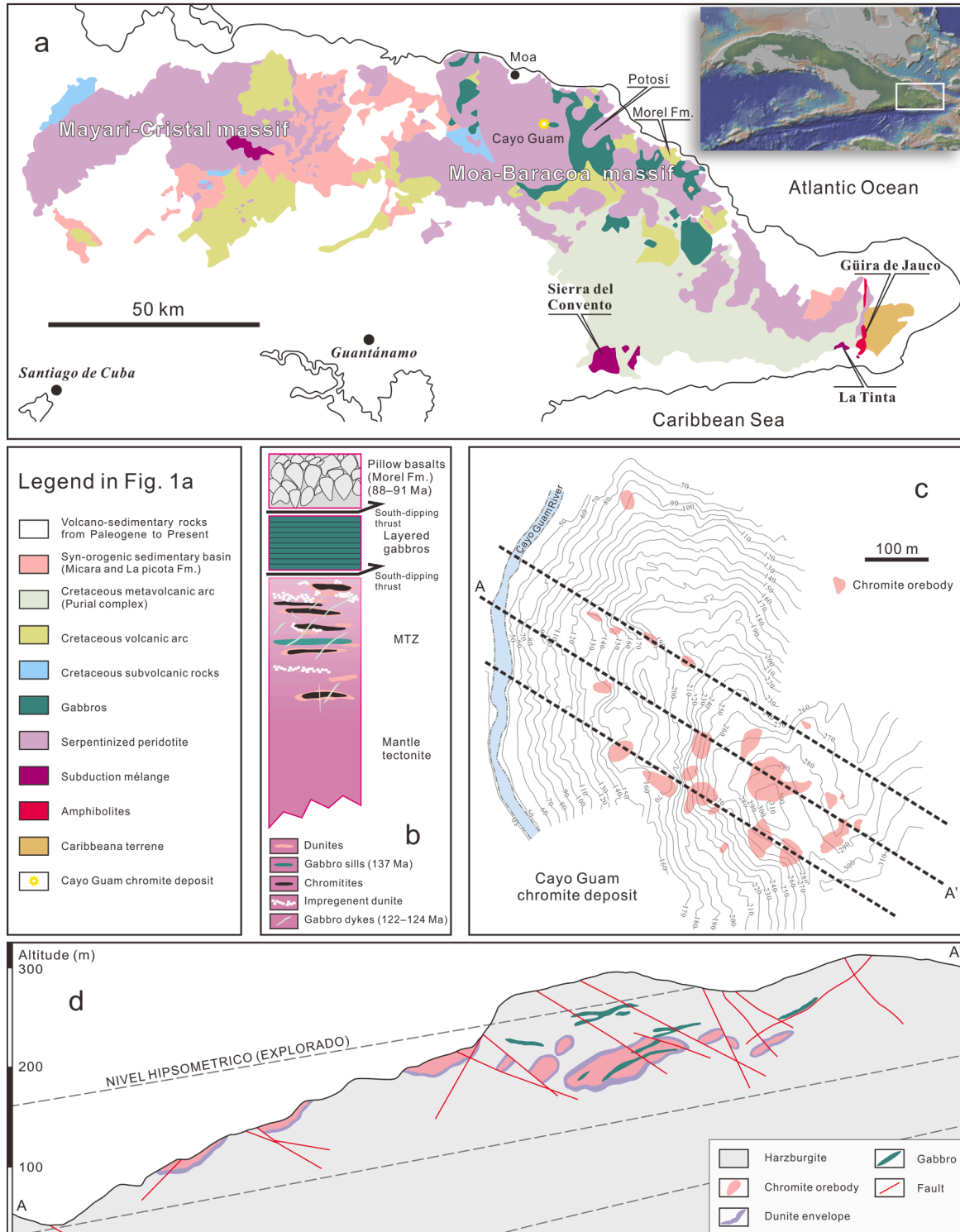
Fig. 1. (**a**) Geological map of eastern Cuba showing the main geological units (after Lázaro et al., 2016); (**b**) Schematic lithostratigraphic columns of the MBOM (after Proenza et al., 2018); (**c**) Geological map of the Cayo Guam chromite deposit; (**d**) Geological profile (A-A') of the Cayo Guam chromite deposit. The ages for ophiolitic rocks in (**b**) are from Iturralde-Vinent et al. (2006), Rojas-Agramonte et al. (2016), and Rui et al. (2022b).

et al., 2017b; Zhang et al., 2020).

High-Cr chromitites usually form in forearc mantle wedges (Ahmed et al., 2020; Nayak et al., 2021; Sepidbar et al., 2021; Sideridis et al., 2021; Uysal et al., 2009; Zhou et al., 1998). Compared to them, the formation of high-Al chromitites is rare and complex. High-Al chromitites are interpreted to originate from MOR (Arai and Miura, 2015; Uysal et al., 2009), back-arc basin (González-Jiménez et al., 2011; Zhu and Zhu, 2020), and nascent forearc during subduction initiation (Rollinson and Adetunji, 2013; Xiong et al., 2017a; Zhang et al., 2020). They usually occur at or above the Moho transition zone (MTZ), such as Nurali chromitites, Urals (Grieco et al., 2007), Kempirsai chromitites, Urals (Melcher et al., 1999), and Kraubath chromitites, Austria (Malitch et al., 2003). The geochemical composition of high-Al chromitites have not yet been well correlated with their geodynamic settings.

The Mayarí-Baracoa ophiolitic belt (MBOB) (eastern Cuba) hosts numerous economically important high-Cr and -Al chromite deposits of variable sizes. Previous studies of chromitites from the MBOB have focused on (1) Re-Os isotope heterogeneities of the upper mantle (Frei et al., 2006; Gervilla et al., 2005; Marchesi et al., 2011); (2) origin of high-Al and -Cr chromitites by melt-rock interaction (González-Jiménez et al., 2011; Proenza et al., 1999; Zhou et al., 2001); (3) unusual minerals (e.g., diamond, moissanite, and zircon) (Proenza et al., 2018; Pujol-Solà et al., 2018, 2020a); and (4) interactions between chromitites and parental melts of gabbro dykes (González-Jiménez et al., 2020; Proenza et al., 2001; Pujol-Solà et al., 2020b). However, investigations focused on the origin of high-Al chromitites in the Moa-Baracoa ophiolitic massif (MBOM) is limited. Here, we present the detailed petrographic observations, mineral chemistry, whole-rock platinum-group element (PGE) geochemistry, and electron backscattered diffraction (EBSD) mapping of chromitites from the MBOM to investigate their petrogenesis and constrain the geodynamic setting of the high-Al chromitites.

2. Geological background

The Northern Cuban ophiolite belt (NCOB) in the west and central part and the MBOB in the east make up the Cuban ophiolites that stretch for >1000 km along the northern margin of Cuba. Both the NCOB and the MBOB comprise of mantle tectonites, plutonic rocks, volcanics, and subduction mélanges (Iturralde-Vinent et al., 2006). The MBOB is separated by fault zones into two individual thrust-bounded blocks, the Mayarí-Cristal ophiolitic massif to the west and the MBOM to the east (Fig. 1a).

The MBOM thrusts over a subduction-related metamorphic complex, and is composed of (from bottom to top) mantle harzburgite tectonite associated with subordinary dunite, a MTZ, and a crustal section made up of cumulate layered gabbros and pillow lavas (Morel Formation) (Fig. 1a, b). The Morel Formation is Turonian–Coniacian (88–91 Ma) in age (Iturralde-Vinent et al., 2006), and separated from the underlying layered gabbros by south-dipping thrusts. The MBOM is generally believed to have formed in a back-arc environment because of the MORB-like geochemical affinity of the Morel Formation (Marchesi et al., 2007; Proenza et al., 2006).

The MBOB hosts numerous economically important chromite deposits. Proenza et al. (1999) classified these deposits into three mining districts: (1) the Moa-Baracoa district in the MBOM; (2) the Sagua de Tánamo district, and (3) the Mayarí district in the Mayarí-Cristal massif. The Moa-Baracoa district contains >100 chromite deposits (Proenza et al., 1999) with estimated reserves of up to 6.5 Mt (Silk, 1988). Among them, the Cayo Guam and Potosí deposits (Fig. 1a) were extensively exploited and have provided an output of >0.8 Mt of ore in the past (Proenza et al., 1999).

3. Field relationships and petrography

The Cayo Guam chromite deposit is situated about 12 km southeast of Moa (Fig. 1a) and contains dozens of orebodies (Fig. 1c, d), which are tabular to lenticular in shape and variable in size. They are hosted in dunitic envelopes within the harzburgite and are concordant with the foliation of the peripheral harzburgite. Gabbro commonly occurs within the chromitite and harzburgite as concordant to sub-concordant intrusives. Additionally, the Cayo Guam chromitites and harzburgites are crosscut by late-stage pegmatitic gabbro dykes. Such dykes have also been reported from the Potosí deposit (González-Jiménez et al., 2014; Proenza et al., 1999; Pujol-Solà et al., 2020b).

Cayo Guam chromitite samples were collected from abandoned ore heaps and pits, and are characterized by predominantly massive and subordinate semi-massive ores. Petrographic characteristics of the chromitites are listed in Table 1. The massive chromitite consists of ≥90% Cr-spinel and minor interstitial silicates (olivine, clinopyroxene, serpentine, and chlorite) (Fig. 2a–c). Samples close to the gabbro dykes have a relatively high mode of interstitial clinopyroxene (3–6%). Cr-spinel generally occurs as large (3–6 mm) anhedral grains. Some have straight grain boundaries and show re-equilibration microstructures, such as 120° triple junctions (Fig. 2b). Abundant monophase and/or polyphase inclusions, including silicates, base-metal sulfides (BMS), and platinum-group minerals (PGM), can be found in Cr-spinel. Silicate inclusions are mainly composed of olivine showing negative crystal shapes against cubic Cr-spinel (Fig. 2d), with minor clinopyroxene and chlorite (Fig. 2e). Generally, the BMS and silicates (e.g., olivine and clinopyroxene) occur together as polyphase inclusions (Fig. 2f). The PGM inclusions are euhedral to subhedral in shape, coexisting with heazlewoodite, amphibole, and secondary chlorite (Fig. 2g–i). Densely exsolved clinopyroxene needles commonly occur in some large Cr-spinel grains. Needles are typically <1 μm wide but up to 150 μm long, and oriented either along three directions (Fig. 3a, b) or one direction (Fig. 3c–g). Secondary inclusion trails were also observed in healed fractures of the large Cr-spinels (Fig. 3h–j). Notably, these healed fractures are slightly deformed (Fig. 3h), indicating overgrowth and deformation after or during fracture healing.

The semi-massive chromitites are made up of 60–90% Cr-spinel and >10% silicates. Interstitial silicates are mainly olivine and serpentine, and no pyroxene was observed. Cr-spinels occur as anhedral small grains (<3 mm) with curved boundaries (Fig. 4a–c). Inclusions in Cr-spinel grains are predominantly composed of olivine, with minor clinopyroxene, phlogopite, and secondary serpentine. Olivine occurs as large (~200 μm) euhedral to anhedral inclusions (Fig. 4d–e). The polyphase inclusions are small (~50 μm), irregularly shaped, and consist of clinopyroxene, orthopyroxene, phlogopite, chlorite (Fig. 4f–h), with rare BMS (Fig. 4i). PGM inclusions, exsolved clinopyroxene needles, triple junctions or healed fractures were not observed in the semi-massive chromitites.

Table 1

Petrological characteristics of the Moa-Baracoa Ti-poor high-Al chromitites.

Sample	Massive chromitite	Semi-massive chromitite
Occurrence	Huge orebody	Small pod in dunite
Silicate matrix	Ol, Cpx	Ol
Spinel mode	≥90%	60–90%
Spinel size	3–6 mm	<3 mm
Spinel morphology	Anhedral	Anhedral
Primary inclusion	Ol, Opx, Cpx, Amp, Pn, Hzl, Ccp, Lrt	Ol, Opx, Cpx, Phl, Hzl, Ccp
Cpx exsolution	Common	Not observed
Healed fracture	Common	Not observed
Secondary inclusion trails	Common	Not observed
Deformation	Strong	Weak to strong
120° triple junctions	Trace	Not observed
Overgrowth	Common	Not observed
Spinel Cr#	50.6–54.7	42.5–47.5
Spinel Mg#	64.1–75.5	65.9–75.3

Amp: amphibole, Ccp: chalcopyrite, Cpx: clinopyroxene, Cr-Spl: Cr-spinel, Hzl: heazlewoodite, Lrt: laurite, Ol: olivine, Pn: pentlandite, Phl: phlogopite.
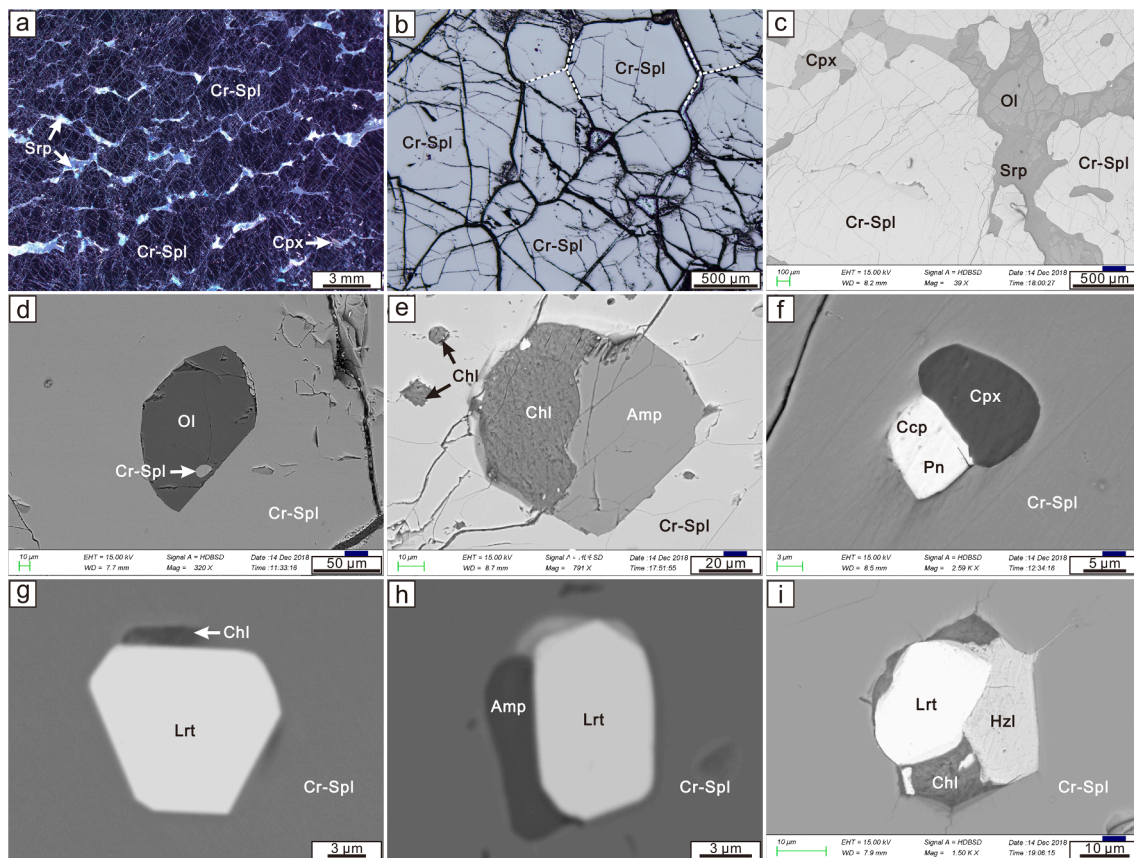
Fig. 2. (**a**, **b**) Photomicrographs and (**c**–**i**) back-scattered electron (BSE) images of the Moa-Baracoa massive chromitites. (**a**) Massive chromitites consisting of >90% Cr-spinel; (**b**) Cr-spinel grains showing triple junctions (reflected light); (**c**) Interstitial olivine and clinopyroxene; (**d**) Olivine inclusion; (**e**) Inclusions of amphibole and chlorite; (**f**) Inclusion of clinopyroxene, pentlandite, and chalcopyrite; (**g**) Euhedral laurite grain; (**h**) Laurite combined with amphibole; (**i**) Laurite coexisting with heazlewoodite. Amp: amphibole, Ccp: chalcopyrite, Chl: chlorite, Cpx: clinopyroxene, Cr-Spl: Cr-spinel, Hzl: heazlewoodite, Lrt: laurite, Ol: olivine, Pn: pentlandite, Srp: serpentine.

Dunitic envelops were dominated by olivine (≥98%) with minor Cr-spinel. Olivine is highly fractured and variably serpentinized. Cr-spinel usually occurs as small (0.5–1.5 mm) anhedral crystals, randomly scattered in the olivine matrix. Peripheral harzburgite comprises olivine (75–85%), orthopyroxene (12–22%), clinopyroxene (<2%), and Cr-spinel (<2%), showing a typical porphyroclastic texture.

4. Analytical methods

The major element compositions of olivine, clinopyroxene, and Cr-spinel were determined using a JEOL JXA-8100 electron probe microanalyzer (EPMA) at the Key Laboratory of Submarine Geosciences, State Oceanic Administration, Hangzhou. Mineral chemistry of the sulfides was determined using a JEOL JXA-iSP100 EPMA at Nanjing Hongchuang Geological Technology Co., Ltd, Nanjing. Analyses (Supplementary Tables S1–S4) were performed at an accelerating voltage of 15 kV, a 20nA beam current, and a 2–5 μm beam spot. The following standards were used for quantification: diopside (Si, Mg, and Ca), rutile (Ti), sanidine (Al, K), rhodonite (Mn), albite (Na), iron oxide (Fe), nickel oxide (Ni), chromium oxide (Cr), marcasite (S), gallium arsenide (As), cuprite (Cu), and pure metals (Co, Os, Ir, Ru, Rh, Pt, and Pd). The approximate detection limit is 0.05% for PGE and 0.01% for the other elements.

The trace element compositions of clinopyroxene and Cr-spinel (Supplementary Tables S5–S6) were analyzed using a Teledyne Cetac Technologies Analyte Excite laser ablation coupled with an Agilent Technologies 7700× quadrupole inductively coupled plasma mass spectrometer (LA-ICP-MS) at the State Key Laboratory of Geological

Processes and Mineral Resources, China University of Geosciences, Wuhan. For each analysis, laser ablation conditions of a spot size of 40 μm, a pulse frequency of 7 Hz, and an energy density of 6.0 J/cm^2 were applied. Basaltic glasses provided by the United States Geological Survey (BIR-1G, BHVO-2G, and BCR-2G) were used as external calibration standards. Off-line data processing was performed by *ICPMSDataCal* software using a 100%-normalization strategy without applying an internal standard (Liu et al, 2008).

Whole-rock PGE (Supplementary Tables S7) was analyzed at the Chinese Academy of Geological Sciences (CAGS). All samples were carefully cleaned, crushed, and ground in an agate mortar to pass through a 200-mesh screen. PGE concentrations were determined using a nickel sulfide fire-assay pre-concentration method followed by ICP-MS analysis. The detailed analytical processes for PGE analysis have been described by Xiong et al. (2017b).

Electron backscattered diffraction (EBSD) was measured using an Oxford Nordlys F+ EBSD detector attached to an FEI Quanta 450 SEM at the CAGS. Crystal orientation mappings were performed at a voltage of 20 kV, a beam current of 180 μA, and step size of 5–9 μm. Automatic indexing and EBSD data processing were performed using *Oxford Instruments AZtec* and *HKL Channel 5*, respectively.
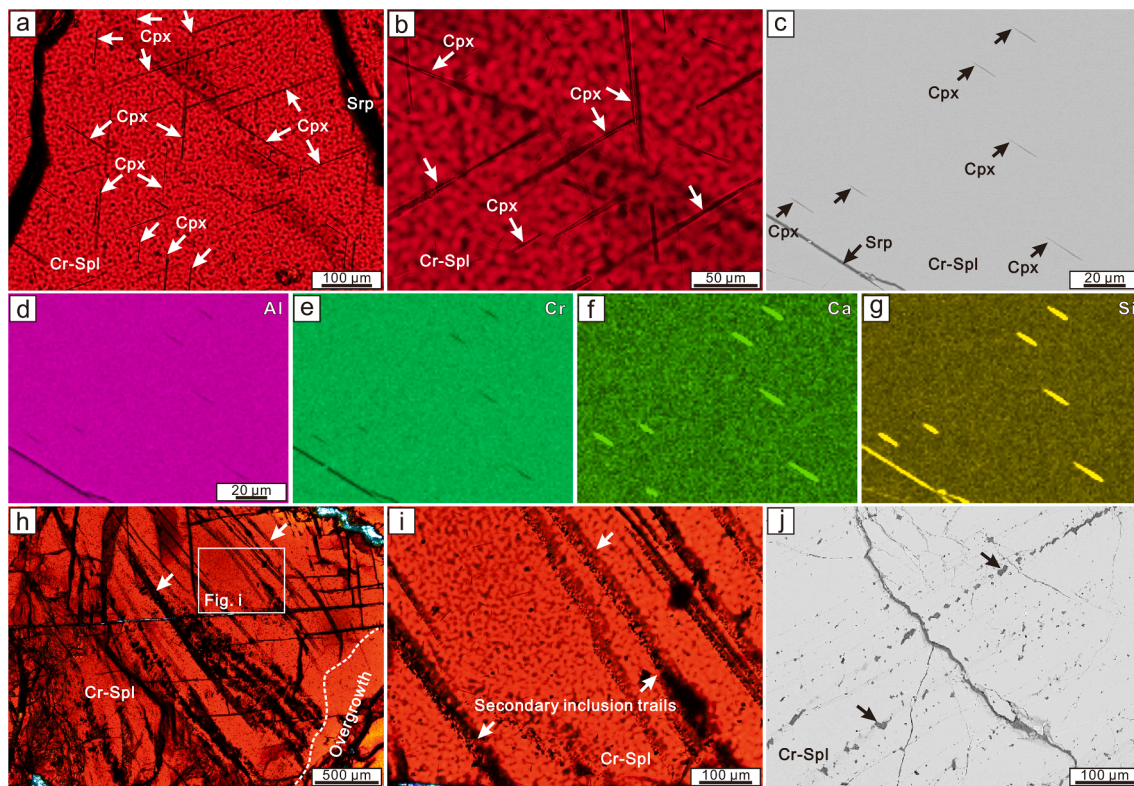
5. Results

5.1. Mineral chemistry

5.1.1. Olivine
Olivine in the dunite and harzburgite have high Fo [100 × Mg/(Mg

Fig. 3. (**a**, **b**) Photomicrographs (transmitted light) and (**c**) BSE image showing exsolved needles of clinopyroxene; (**d**–**g**) Energy dispersive spectrometer element mapping in the same area of (**c**); (**h**) Photomicrographs (transmitted light) showing overgrowth after fracture healing; (**i**) Photomicrographs (transmitted light) and (**j**) BSE image showing healed fractures illustrated by secondary inclusion trails. Cpx: clinopyroxene, Cr-Spl: Cr-spinel, Srp: serpentine.

+ Fe^{2+}] values (89.9–93.4) and NiO contents (0.29–0.51 wt%), with low MnO contents (0.05–0.21 wt%), consistent with olivine mantle array (Fig. 5a, b). In contrast, olivine in the chromitites show remarkably higher Fo values (94.6–97.2) and NiO contents (0.48–1.12 wt%), with slightly lower MnO contents (~0.12 wt%) (Fig. 5a, b). Notably, the olivine inclusions in Cr-spinel show comparatively higher Fo values and NiO contents, with significantly higher Cr_2O_3 contents relative to the matrix olivine of the studied chromitite samples (Fig. 5a, c).

5.1.2. Clinopyroxene

Clinopyroxenes in massive chromitites and peripheral harzburgites have similar Al_2O_3 (1.85–3.14 wt%) and TiO_2 (0.01–0.11 wt%) contents. However, the Mg# values (94.6–96.1) and Na_2O contents (0.27–0.46 wt%) of clinopyroxenes in chromitites are relatively higher (Fig. 5d–f). Moreover, the clinopyroxenes in chromitites have higher total rare earth elements (ΣREE = 12.3–21.3 ppm) than of those in the harzburgites (ΣREE = 0.24–0.49 ppm). In the chondrite-normalized plot, their REE patterns show depletion in light REE (La_N/Lu_N = 0.09–0.13) (Fig. 6a). In the primitive mantle-normalized multi-element diagram, chromitite clinopyroxenes show strongly negative anomalies for Pb, Sr, and Ti, which differ from those of harzburgite clinopyroxenes that display positive Pb and Ti anomalies (Fig. 6b).

5.1.3. Cr-spinel

Cr-spinel grains are usually chemically homogenous, and have narrow ranges of major- and trace-element compositions in an individual lithology. Cr-spinel in the massive chromitites have Cr# (50.6–54.7), Mg# (64.1–75.5), Al_2O_3 (24.61–27.05 wt%), Cr_2O_3 (40.93–44.94 wt%), MgO (14.10–17.05 wt%), FeO (12.56–16.49 wt%), and TiO_2 (0.02–0.13 wt%) (Fig. 7). Cr-spinels in semi-massive chromitites display comparatively lower Cr# (42.5–47.5), but similar Mg# (65.9–75.3) and TiO_2 (0.05–0.15 wt%) relative to massive chromitites. According to their Cr# values, the studied chromitites were classified as high-Al type (Fig. 7a)

(Rollinson, 2008; Zhou et al., 2014). Cr-spinels in the dunite envelopes are characterized by low Cr# (41.3–48.9) but high Mg# (65.7–71.9), similar to those from both chromitites. However, Cr-spinels in the harzburgites have the highest Cr# (53.7–62.3) and lowest Mg# (54.9–60.2), which deviates from the general chromitite-dunite associations (Fig. 7a).

Because Ga is hardly affected by re-equilibration processes (Economou-Eliopoulos et al., 2019), trace element abundances were plotted against Ga in Fig. 8. The abundances of Ga decrease with increasing Cr# values. Cr-spinels in the chromitites have higher Ga contents (50.8–62.2 ppm) than those of the dunites (33.7–44.8 ppm) and harzburgites (23.1–38.2 ppm). Ga displays a positive correlation with Ti, and Ni, and a negative correlation with Co, Mn, and V (Fig. 8a–e). In the MORB spinel-normalized multi-element diagrams, Cr-spinels of the massive and semi-massive chromitites show roughly similar patterns as in typical high-Al chromitites, except for clearly negative anomalies of Ti and Sc (Fig. 9a). The Cr-spinels of dunites and harzburgites show variable depletion of Ti and Sc, and enrichment of Zn and Co relative to MORB spinel (Fig. 9b). It is noteworthy that the Moa-Baracoa high-Al chromitites are quite poor in Ti relative to the typical high-Al chromitites worldwide (Fig. 8a, 9a). Thus, we define these chromitites as Ti-poor high-Al chromitites.

5.1.4. BMS and PGM

The EPMA data for BMS and PGM are listed in Supplementary Tables S4. Heazlewoodite, pentlandite, and chalcopyrite are the most abundant phases among BMS. Heazlewoodite is characterized by high Ni (69.23–72.36 wt%) and low S (26.64–27.60 wt%) contents. Pentlandite has an almost consistent amount of Ni (38.29–39.01 wt%), Fe (24.97–27.36 wt%), and S (33.11–33.56 wt%). Chalcopyrite is composed of Cu (32.95 wt%), Fe (29.72 wt%), and S (34.88 wt%).

Eight laurite grains were observed after studying >100 thin sections. It was the only PGM phase observed in this study, and consists of Os
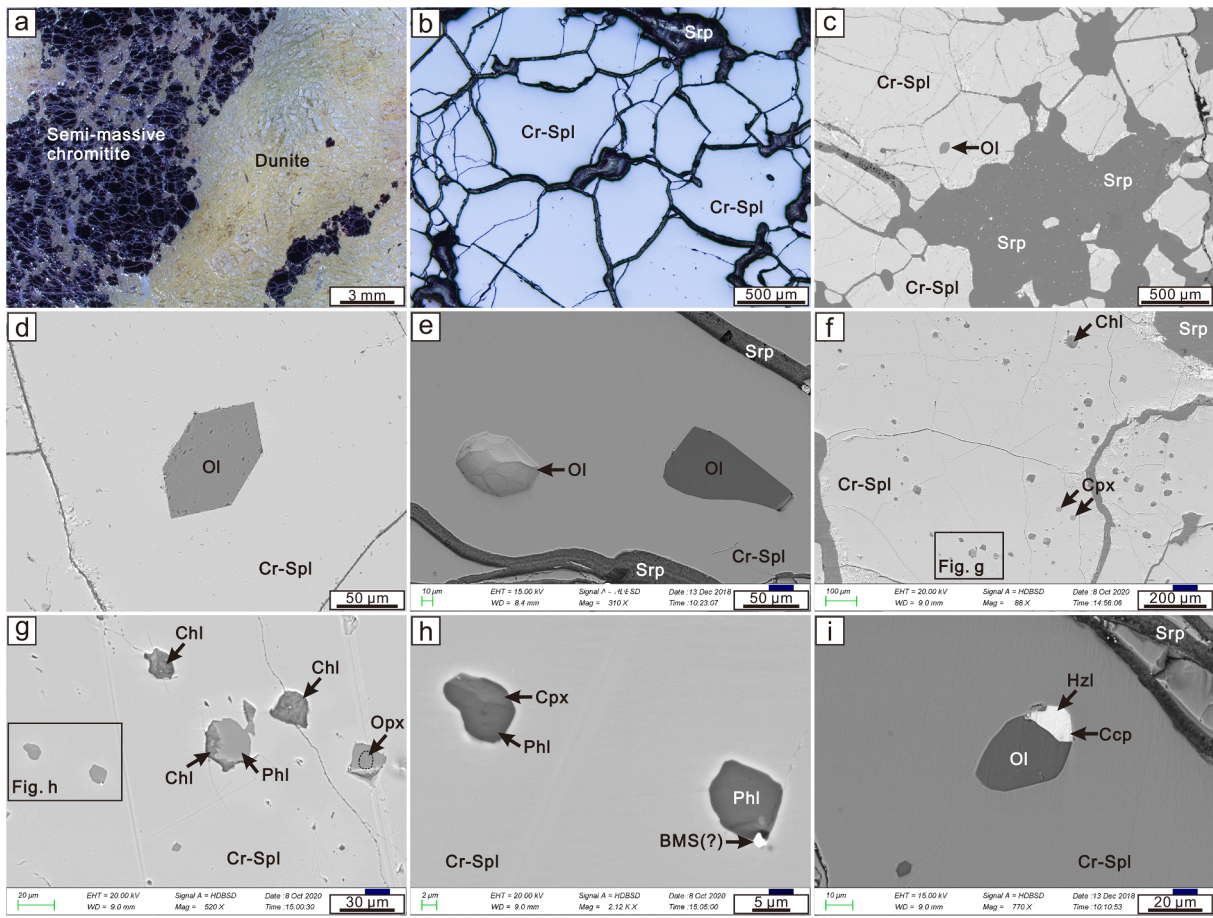
Fig. 4. (**a**, **b**) Photomicrographs and (**c–i**) BSE images of the Moa-Baracoa semi-massive chromitites. (**a**) Semi-massive chromitites consisting of 60–90% Cr-spinel; (**b**) Anhedral Cr-spinel grains with curved boundaries (reflected light); (**c**) Primary interstitial silicate completely replaced by serpentine; (**d**, **e**) Euhedral and subhedral olivine inclusions; (**f–h**) Pyroxene and phlogopite inclusions; (**i**) Olivine combined with chalcopyrite and heazlewoodite. BMS: base-metal sulfide, Ccp: chalcopyrite, Chl: chlorite, Cpx: clinopyroxene, Cr-Spl: Cr-spinel, Hzl: heazlewoodite, Ol: olivine, Phl: phlogopite, Srp: serpentine.
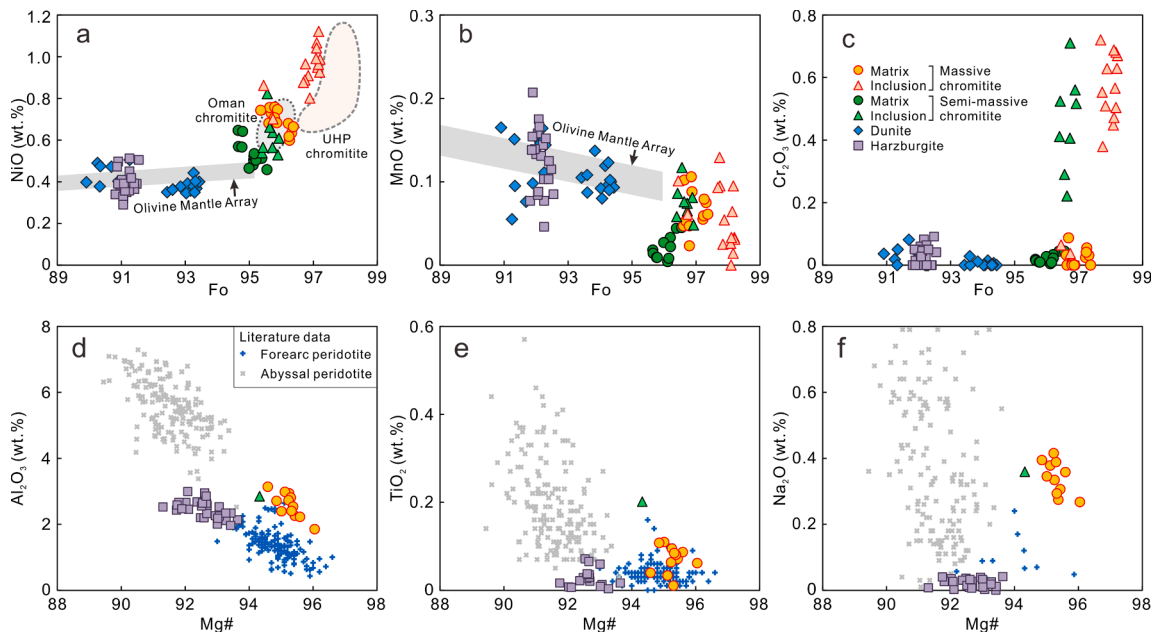
Fig. 5. Compositional plots of (**a–c**) NiO, MnO, and Cr_2O_3 contents vs. Fo values of olivine, and (**d–f**) Al_2O_3, TiO_2, and Na_2O contents vs. Mg# values of clino-pyroxenes from the MBOM. The olivine mantle array is from Takahashi et al. (1987). UHP and Oman chromitites are from Arai and Miura (2016). Forearc peridotite data are from Ishii et al. (1992) and Birner et al. (2017); Abyssal peridotite data are from Brunelli et al. (2006) and Seyler et al. (2003).
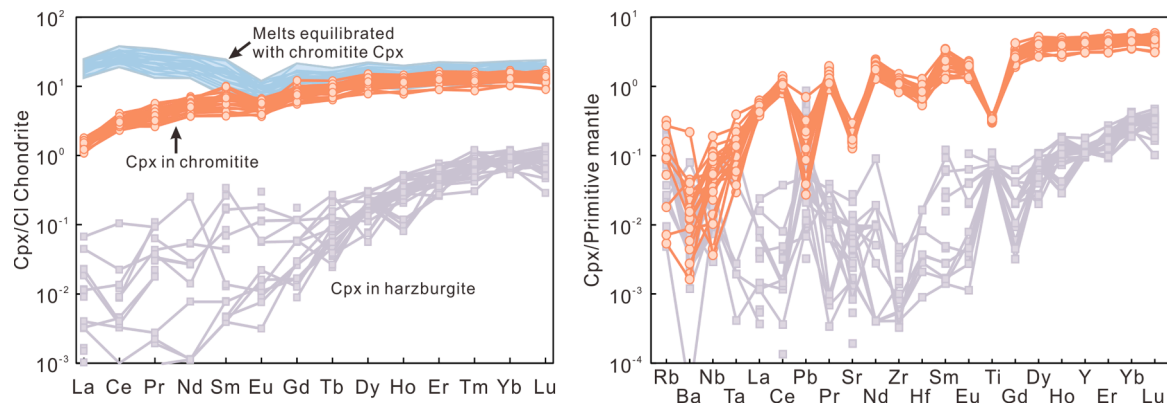
Fig. 6. (**a**) Chondrite-normalized REE and (**b**) Primitive mantle-normalized multi-element diagrams of clinopyroxene from massive chromitites and harzburgite of the MBOM. Harzburgite data are from Rui et al. (2021). Chondrite and primitive mantle normalizing values are from Sun and McDonough (1989). Clinopyroxene/melt partition coefficients are from Sun and Liang (2012).

(22.22–35.23 wt%), Ru (19.25–38.59 wt%), Ir (2.54–11.09 wt%), and S (29.73–34.82 wt%). The compositional range of laurite is narrow (Fig. 10), with Ru# [Ru/(Ru + Os)] spanning from 0.51 to 0.77.

5.2. Whole-rock PGE geochemistry

Five massive and one semi-massive chromitite samples from the MBOM were analyzed for whole-rock PGE abundance. Their total PGE (ΣPGE) concentrations range between 56 and 122 ppb. The whole-rock PGE abundances of both types (massive and semi-massive) were similar, characterized by enrichments in IPGE relative to PPGE as manifested by the low Pd/Ir (0.13–0.31) and PPGE/IPGE (0.06–0.13) ratios (Fig. 11). Moa-Baracoa chromitites generally have a PPGE-depleted chondrite-normalized pattern. Additionally, they show weak positive anomalies of Os and Ru with respect to Ir (Fig. 12). Such double peak patterns are consistent with the presence of laurite as the only PGM phase in the studied samples. Moreover, previous reported high-Al chromitites also show double peak patterns for PGEs (Fig. 12b, c).

5.3. Microstructures

The microstructures of two massive and two semi-massive chromitites were examined by EBSD analysis. EBSD mapping reveals that the Cr-spinel grains of the Moa-Baracoa chromitites suffered weak to strong crystal-plastic deformation. Some large Cr-spinel grains with exsolved clinopyroxene needles in the massive chromitites show strong crystal-plastic deformation, and are composed of coalescent Cr-spinel sub-grains (Fig. 13a, b). In the semi-massive chromitites, Cr-spinel crystals display weak to strong crystal-plastic deformation; however, no sub-grains were identified inside them (Fig. 13c–e).

6. Discussion

6.1. Low- and high-pressure fingerprints in the Moa-Baracoa high-Al chromitites

Podiform chromitites are traditionally interpreted to have originated from low-pressure (LP) magmatism within the upper mantle (e.g., Arai, 2013, and references therein). However, substantial ultrahigh-pressure (UHP) to high-pressure (HP) mineralogy reported in some ophiolitic peridotites and podiform chromitites, such as *in situ* and separated diamonds (Rui et al., 2022a;Yang et al., 2007, 2021), coesite exsolutions (Yamamoto et al., 2009), clinopyroxene exsolutions (González-Jiménez et al., 2017; Xiong et al., 2017a; Yamamoto et al., 2009), and calcium amphibole exsolutions (Chen et al., 2019) in Cr-spinel, provide important clues for understanding the formation of podiform chromitites and mantle dynamics in a larger scale (e.g., Arai, 2013; Yang et al., 2015;
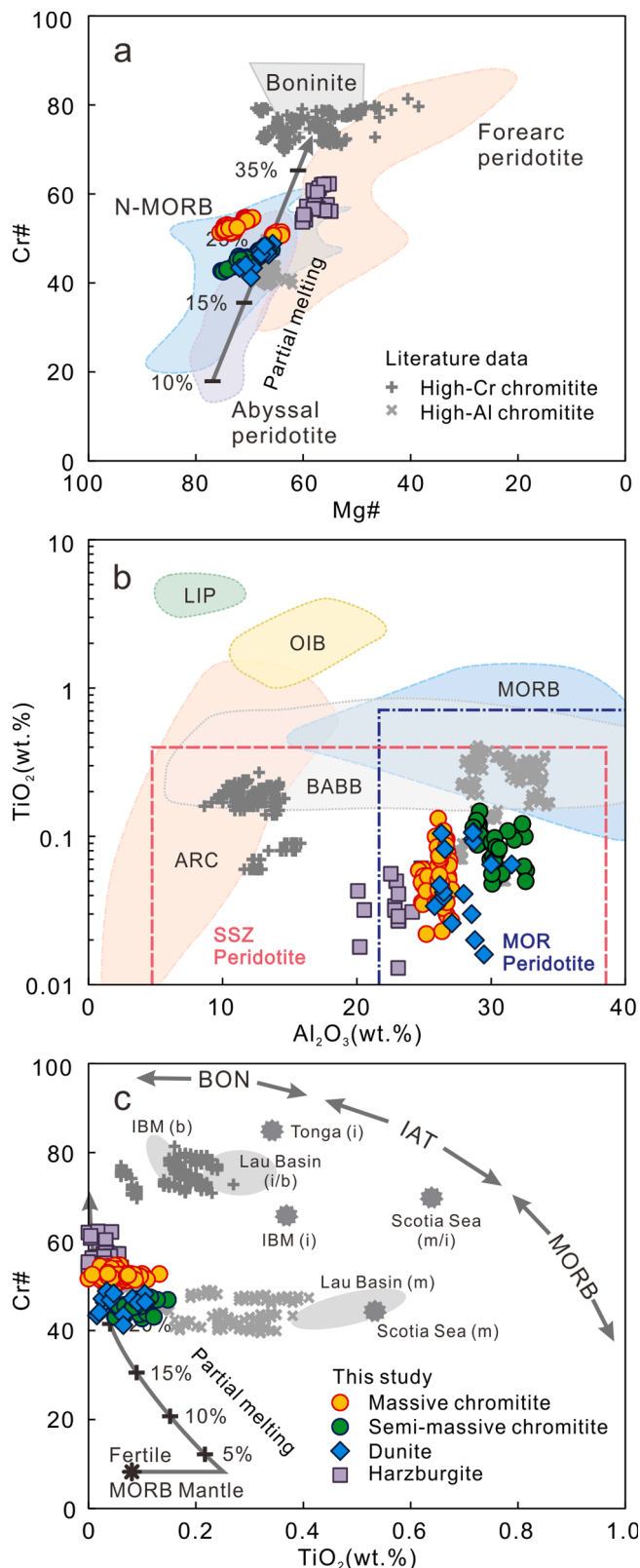
Zhou et al., 2014).

In the MBOM, LP fingerprints occur in both the massive and semi-massive chromitites. For example, small amounts of primary hydrous mineral inclusions, such as amphibole and phlogopite, are hosted within the Cr-spinel (Fig. 2e, h, 4f–h), which resembles the LP chromitites formed by melt-rock interaction in the shallow mantle (e.g., Arai and Miura, 2016; Xiong et al., 2017a). Experiments have demonstrated that pargasite is unstable at >3 GPa and ~1150 °C (Niida and Green, 1999).

Among the Moa-Baracoa chromitites, HP fingerprints only occur in massive variety. Abundant clinopyroxene needles with strong crystallographic preferred orientations were commonly exsolved within some Cr-spinel grains (Fig. 3a–g). Such microstructures have been regarded as indicators for HP conditions (Yamamoto et al., 2009), and were reported from the UHP-HP chromitites of Tibet (Xiong et al., 2017a; Yamamoto et al., 2009), Oman (Miura et al., 2012), and Mexico (González-Jiménez et al., 2017). Experiments have demonstrated that magnesiochromite transforms into a $CaFe_2O_4$ structure (CF-type) above 12.5–18 GPa (Chen et al., 2003; Wu et al., 2016; Zhang et al., 2017a, Zhang et al., 2017b), and to a $CaTi_2O_4$ structure (CT-type) above 20 GPa (Chen et al., 2003; Zhang et al., 2017a, Zhang et al., 2017b). The CF-type spinel can incorporate high contents of SiO_2 (~3–5 wt%) and CaO (~7–8 wt%) at 14–18 GPa, whereas magnesiochromite comparatively incorporates a minor amount of SiO_2 (<1–2 wt%) and almost no CaO at 12–16 GPa (Zhang et al., 2017a, Zhang et al., 2017b). Additionally, the SiO_2 content accommodated in magnesiochromite increases from 0.1 to 0.7 wt% with increasing pressure from 5 to 12 GPa at a temperature of 1400 °C (Wu et al., 2016). Therefore, abundant clinopyroxene exsolution needles in Cr-spinel have been interpreted as a result of decompression from the CF-type or HP magnesiochromite to the LP phase (Arai, 2013; González-Jiménez et al., 2017; Satsukawa et al., 2015; Xiong et al., 2017a; Yamamoto et al., 2009).

Compared to the semi-massive chromitites, the Fo values and NiO contents of olivine inclusions are higher in massive chromitites, which are comparable with those of olivines from UHP chromitites in Tibet (Fig. 5a). Similar trends have been widely reported in ophiolitic podiform chromitites, and are ascribed to the Fe-Mg exchange between included olivine and host Cr-spinel (e.g., Bussolesi et al., 2019; Rui et al., 2019; Sideridis et al., 2021). Such high Fo values and NiO contents in the studied samples suggest that the massive chromitites were subject to considerably intensive exchange processes. The olivine-spinel geothermometer (Ballhaus et al., 1991) yields almost similar temperatures for the semi-massive (549–687 °C) and massive samples (551–705 °C). Given the intensive Fe-Mg exchange between olivine and Cr-spinel, the calculated temperatures imply that the semi-massive and massive chromitites experienced similar re-equilibration processes under low pressure and temperature.

EBSD maps of the massive chromitites show that the large Cr-spinel

Fig. 7. Plots of (**a**) Cr# vs. Mg#, (**b**) TiO_2 vs. Al_2O_3, and (**c**) Cr# vs. TiO_2 of Cr-spinel from the MBOM. High-Cr and -Al chromitite data are from Zhou et al. (2014). The diagram (**a**) is modified after Dubois-Côté et al. (2005), diagram (**b**) after Kamenetsky et al. (2001), and diagram (**c**) after Pearce et al. (2000). The subscripts b, i and m denote boninite, island arc tholeiite and MORB, respectively.

grains with crystal-plastic deformation were composed of coalescent subgrains (Fig. 13a, b). Similar deformation textures have been observed in the Luobusa and Zedang massive chromitites, and were interpreted to be the result of HP/high-temperature (HP/HT) metamorphism in the deep mantle (Griffin et al., 2016; Satsukawa et al., 2015; Xiong et al., 2017a). Furthermore, 120° triple junctions (Fig. 2b), healed fractures, and considerable overgrowth of Cr-spinel after fracture healing (Fig. 3h, i) suggest complex metamorphic processes in HP/HT conditions. Therefore, it is inferred that both low- and high-pressure processes were involved in the formation of the Moa-Baracoa chromitites.

6.2. Petrogenetic implication from the PGE, PGM, and BMS

The distribution of PGE is sensitive to the inventories and S-saturation status of parental magmas (Barnes et al., 1985; Naldrett and von Gruenewaldt, 1989); thus, it can provide unique insights into the formation of podiform chromitites (Ahmed and Arai, 2002; Proenza et al., 1999; Shi et al., 2007; Uysal et al., 2018; Zhou et al., 1998). Hydrothermal alteration is common in podiform chromitites, which might cause PGM desulfurization and PGE remobilization (Grieco et al., 2007, 2020). Although the studied samples contain serpentine, chlorite, and Fe-chromite, which are common secondary phases produced during hydrothermal events (Grieco et al., 2020; Merlini et al, 2009; Rui et al., 2019), the following evidence suggests that hydrothermal alteration has little influence on the PGM and PGE distribution of the Moa-Baracoa chromitites: (1) Laurite grains occur as inclusions within Cr-Spinel, and do not show *in situ* alteration, such as formation of PGE-alloys or chemical zoning (Grieco et al., 2020); (2) BMS, such as heazlewoodite, usually have no detectable PGE (Supplementary Table S4), resembling those transformed from magmatic pentlandites (Grieco et al., 2020); (3) while Cr-spinel grains in some semi-massive chromitites are partially replaced by Fe-chromite at rims and along fractures (Fig. 4c), the massive samples are completely free of Fe-chromite, implying a low degree of alteration; (4) chlorite commonly coexists with primary amphibole and phlogopite (Fig. 2e, 3 g), indicating low-temperature hydrothermal alteration.

Global PGE data of both high-Cr and -Al podiform chromitites hosted in Phanerozoic ophiolites were compared with the Moa-Baracoa chromitites (this study). The ΣPGE of the previously reported chromitites is highly variable, ranging from tens to thousands of ppb (Fig. 11b). Although the high-Cr chromitites have an overall slightly higher ΣPGE (average = 259 ppb, n = 288) than the high-Al variety (average = 118 ppb, n = 88), they still show considerable overlapping spectra (Fig. 11b). In the chondrite-normalized PGE patterns, high-Cr chromitites display uniformly significant depletion of PPGE relative to IPGE (Fig. 12a). Such distinguishing features are also shown by the ratios of Pd/Ir, Pt/Pt* [$Pt_N/(Rh_N \times Pd_N)^{1/2}$], and PPGE/IPGE, which are significantly <1 (Fig. 11). In contrast, the high-Al chromitites show either weak depletion or enrichment of PPGE compared with IPGE (Fig. 12b), with highly variable ratios of Pd/Ir (0.02–40.20) and PPGE/IPGE (0.06–10.87) (Fig. 11).

Since IPGE are more refractory during partial melting and also more compatible during fractional crystallization compared to PPGE (Barnes et al., 1985), the Pd/Ir ratios would increase with decreasing Pt/Pt* values in a fractionating magma (Garuti et al., 1997). The Moa-Baracoa chromitites have low Pd/Ir (0.22–0.69) and PPGE/IPGE (0.06–0.13) ratios, with PPGE-depleted patterns (Fig. 12c). The narrow variation of Pd/Ir and Pt/Pt* suggests that PGE distribution in the Moa-Baracoa chromitites was predominately controlled by partial melting rather than magma fractionation (Fig. 11a).

The degree of partial melting chiefly governs the extraction of PGE from mantle sources into the melts (Hamlyn and Keays, 1986). Magmatic PGE concentrations of chromitites are controlled by the nature of their parental melts. Namely, boninitic melt derived from high-degree (≥20%) melting precipitates high-PGE chromitites, whereas basaltic melts produced by ≤20% partial melting crystallize low-PGE
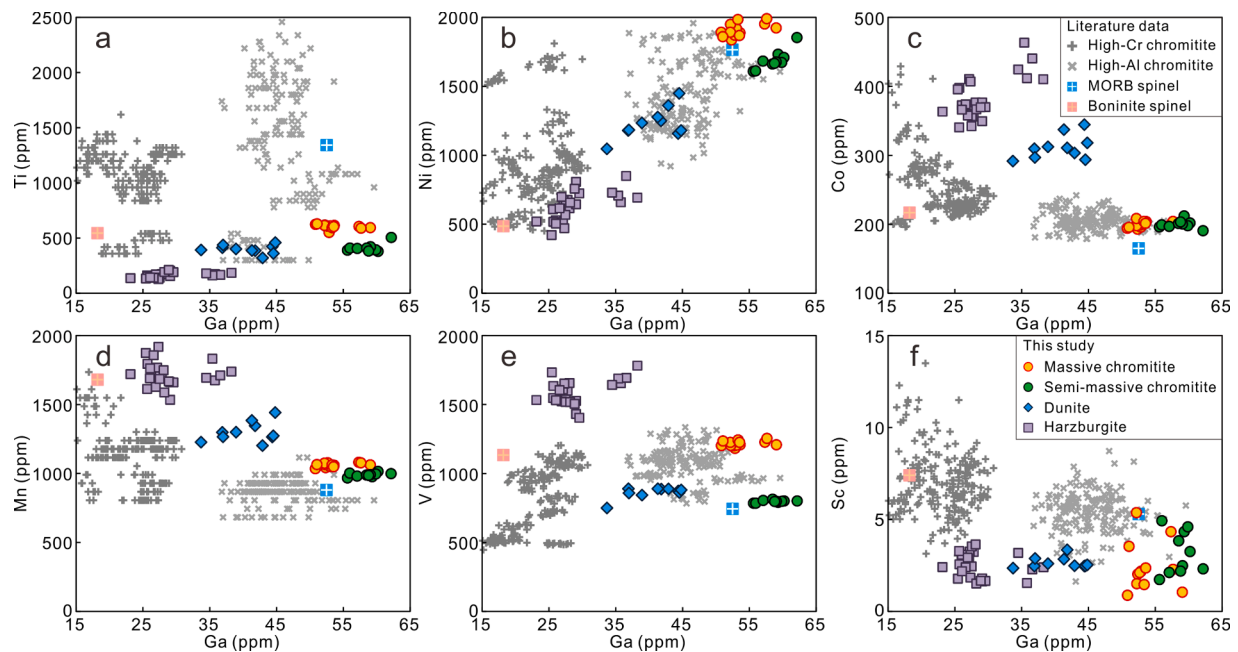
Fig. 8. Compositional plots of Ti, Ni, Co, Mn, V, and Sc vs. Ga of Cr-spinel from the MBOM. Harzburgite data are from Rui et al. (2021). High-Cr and -Al chromitite data are from Zhou et al. (2014); MORB and boninite spinel data are from Pagé and Barnes (2009).
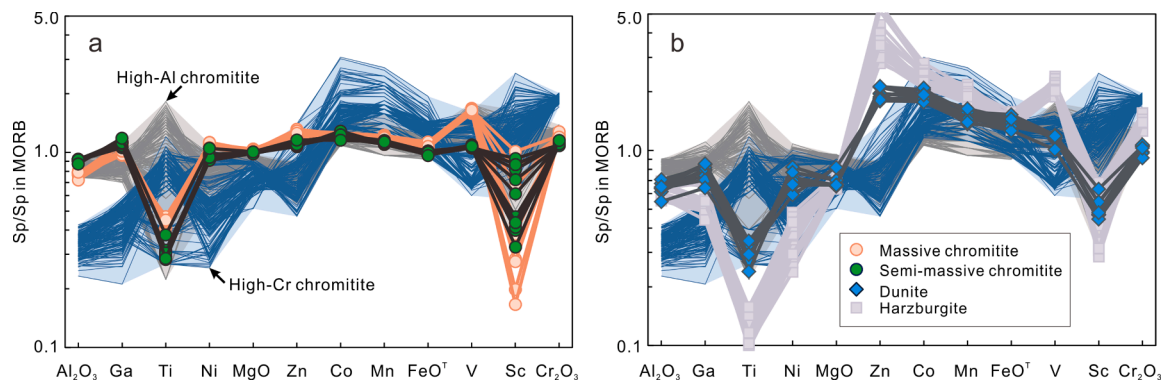
Fig. 9. MORB spinel-normalized (Pagé and Barnes, 2009) multi-element patterns of Cr-spinel from the MBOM. Harzburgite data are from Rui et al. (2021). Blue and grey shaded areas represent the composition range of high-Cr and -Al chromitites, respectively. Data of the high-Cr and -Al chromitite are from Zhou et al. (2014).

chromitites (Peighambari et al., 2016; Prichard et al., 2008). The Moa-Baracoa chromitites contain ΣPGE of 56–122 ppb, falling in the overlapping field of global Phanerozoic high-Cr and -Al chromitites (Fig. 11b). The low PPGE/IPGE ratios of the Moa-Baracoa chromitites indicate that their parental magma was derived from a depleted mantle source where PPGE had already been partly extracted during a previous partial melting event (e.g., Peighambari et al., 2016).

The PGE of ophiolitic chromitites predominantly reside in accessory PGMs that are dominated by Os-Ir alloy and Ru-Os disulfides (Garuti et al., 1999; Gervilla et al., 2005; González-Jiménez et al., 2014; Sideridis et al., 2021; Uysal et al., 2015). The precipitation of PGM and BMS in mafic melts is mainly controlled by sulfur fugacity and temperature (Akmaz et al., 2014; Melcher et al., 1997; Uysal et al., 2015). Laurite and Os-Ir alloys coprecipitate at high temperature (1300 °C) and low fS_2 (log$fS_2 \approx -2$) conditions; as the temperature decreases to 1000 °C and sulfur fugacity increases to log$fS_2 \approx +2$, BMSs start to crystallize from the melts (Uysal et al., 2015). The laurite with high Os content (Fig. 10) can be related to evolved melts with relatively low temperature and/or high fS_2 (Grieco et al., 2020). Abundant BMS inclusions in the Moa-Baracoa chromitites might be indicative of high fS_2 (Uysal et al., 2015). The occurrence of PGMs and BMSs in a single chromitite sample,

especially the coexistence of laurite and pentlandite (replaced by heazlewoodite), indicates rapid and significant local variations in temperature and fS_2. Such physicochemical fluctuations may result from melt-rock interaction and subsequent influx of different melts (Arai and Yurimoto, 1994; Arai and Miura, 2016; González-Jiménez et al., 2014). Moreover, Gervilla et al. (2005) and Frei et al. (2006) have documented that the Moa-Baracoa high-Al chromitites have heterogeneous Os isotopic compositions, indicating mixing/mingling of different magma (Gervilla et al., 2005).

6.3. Formation process of the Moa-Baracoa Ti-poor high-Al chromitites

6.3.1. Composition of parental magmas

Podiform chromitites are Cr-spinel cumulates deposited in magma conduits within mantle peridotites (e.g., Arai and Miura, 2016; Zhou et al., 2014). The chemistry of Cr-spinel reflects the composition of their parental melts (e.g., Dick and Bullen, 1984; Pagé and Barnes, 2009). We calculated the Al_2O_3 and TiO_2 contents, and FeO/MgO ratios for the parental melts of the chromitites using the equations of Rollinson (2008) and Maurel and Maurel (1982), respectively. The parental melts of the Moa-Baracoa chromitites have high Al_2O_3 content (15.5–16.7 wt%) that
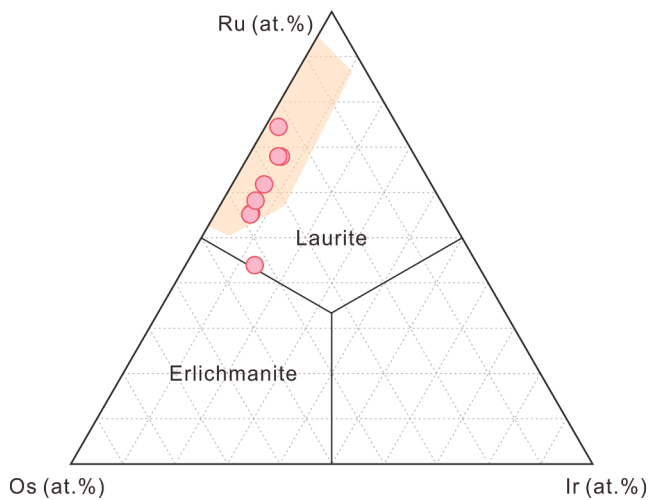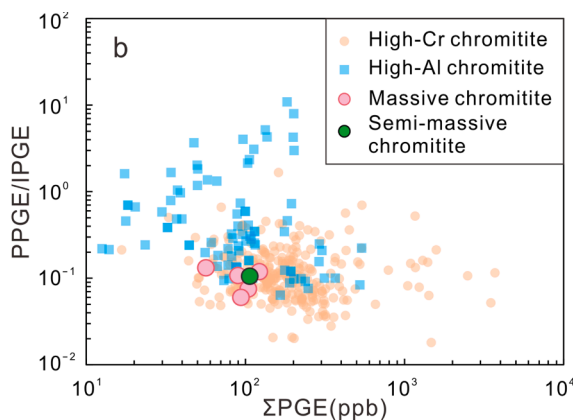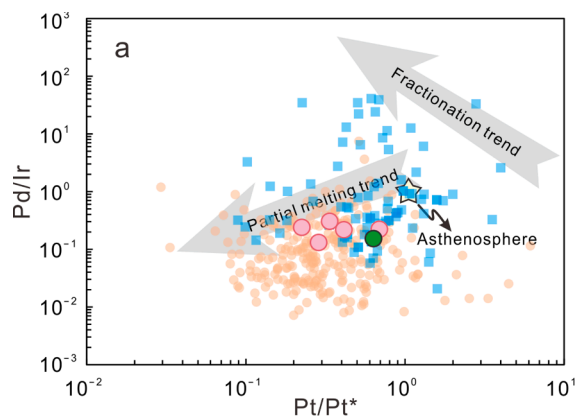
Fig. 10. Ternary compositional diagram of PGM in the Moa-Baracoa high-Al chromitites. Colored field represents compositional range of laurite from the Mayarí-Cristal massif (González-Jiménez et al., 2011).

is concordant with MORB, but low TiO$_2$ content (0.07–0.48 wt%) and FeO/MgO ratios (0.75–1.18), which is similar to boninite-like magmas (Fig. 14a).

Trace element contents for the parental melts of Cr-spinel were estimated using the empirical partition coefficients of Pagé and Barnes (2009). In the MORB-normalized trace element diagram (Fig. 14b), the calculated parental melts generally have flat patterns from V to Ga, which is comparable to those in MORB (Pagé and Barnes, 2009; Zhou et al., 2014). However, they show strikingly depleted Ti relative to other trace elements (Fig. 14b), which is typical of boninite-like melts. Additionally, melts equilibrated with interstitial clinopyroxene in the massive chromitites are calculated using Cpx/melt partition coefficients proposed by Sun and Liang (2012). The results show slight enrichment of light REE and depletion of Eu in the chondrite-normalized REE diagram (Fig. 6a). This indicates that these clinopyroxenes precipitated from residual melts after crystallization of plagioclase, and they may not be syngenetic with the massive chromitites.

6.3.2. Nature of magma source

Ti-poor high-Al chromitites have also been reported from the Zambales ophiolite, Philippines (TiO$_2$ = 0.05–0.22 wt%, Zhang et al., 2020).

Using batch and fractional partial melting models, Zhang et al. (2020) modeled the mantle source and TiO$_2$ content for the parental magma of the Zambales chromitites. A high degree of partial melting (~10% melt extraction from a fertile MORB mantle followed by a second stage of 5–10% partial melting) is necessary to produce low TiO$_2$ (<0.5 wt%) parental magma (Zhang et al., 2020). Thus, we infer that the parental magma of the Moa-Baracoa high-Al chromitites probably resulted from a relatively high degree partial melting of a mantle source: (1) Parental magma has transitional composition between MORB and boninite-like melt with very low TiO$_2$ (0.07–0.48 wt%), which is generally produced by a high degree of partial melting (Zhang et al., 2020); (2) low PPGE/IPGE ratios and relatively high PGE concentrations indicate a previous depleted mantle source; (3) Harzburgites of the MBOM have experienced a high degree (>25%) of partial melting (Marchesi et al., 2006; Rui et al., 2021).

The fO$_2$ of the Moa-Baracoa harzburgites, dunites, and chromitites were estimated using the compositions of the paired Cr-spinel and olivine (Ballhaus et al., 1991). The harzburgites and dunites have considerably lower Δlog$f$O$_2$(FMQ) values (−1.4 to −0.5) compared with chromitites (−0.7 to +1.8) (Fig. 15). Most of the chromitites fall within the subarc mantle field, whereas the dunite and harzburgites spread close to the field of abyssal peridotites in the diagram of Δlog$f$O$_2$(FMQ) vs. Cr# of Cr-spinel (Fig. 15), indicating that parental magma of the chromitites is more oxidized than typical MORB magmas and has an arc affinity.

Subduction-related lavas and peridotites have overall higher fO$_2$ than their MOR counterparts, which are generally ascribed to the modification of slab-derived materials (Birner et al., 2017). High fO$_2$ values recorded in the investigated chromitites might imply that small amounts of slab-derived high-fO$_2$ materials were involved in the mantle source of the parental magma (Zhang et al., 2020). Proenza et al. (2018) identified abundant crustal zircons in the Moa-Baracoa chromitites. Such occurrences combined with high fO$_2$ of the chromitites suggests that the mantle source of the Moa-Baracoa chromitites was contaminated by subducted crustal materials (e.g., González-Jiménez et al., 2017; Lian et al., 2020; Robinson et al., 2015). Collectively, we infer that a forearc mantle contaminated by subducted crustal materials is the probable mantle source for the parental magma of the Moa-Baracoa chromitites.

6.3.3. Crystallization of Cr-spinel

Melt-rock interactions and subsequent mixing/mingling of melts play a critical role in the formation of podiform chromitites (Arai and

Fig. 11. (a) Pt/Pt* vs. Pd/Ir and (b) ΣPGE vs. PPGE/IPGE of the chromitite. Fractionation and partial melting trends, and primitive asthenosphere composition are from Garuti et al. (1997). Pt/Pt* = Pt$_N$/(Rh$_N$ × Pd$_N$)$^{1/2}$. Chondrite normalizing values are from Anders and Grevesse (1989). High-Cr and -Al chromitite data are from Ahmed and Arai (2002), Gervilla et al. (2005), González-Jiménez et al. (2011), Günay and Çolakoğlu (2016), Habtoor et al. (2017), Ismail et al. (2010, Ismail et al., 2014), Lian et al. (2015, Lian et al., 2019), Peighambari et al. (2016), Proenza et al. (1999), Qiu et al. (2018), Sideridis et al. (2021), Ullah et al. (2020a, Ullah et al. (2020b), Uysal et al. (2009, Uysal et al., 2016,Uysal et al., 2018), Wu et al. (2019), Xiong et al. (2017b, Xiong et al. 2018, Xiong et al. 2020, Xiong et al. 2021), Zhou et al. (1998).
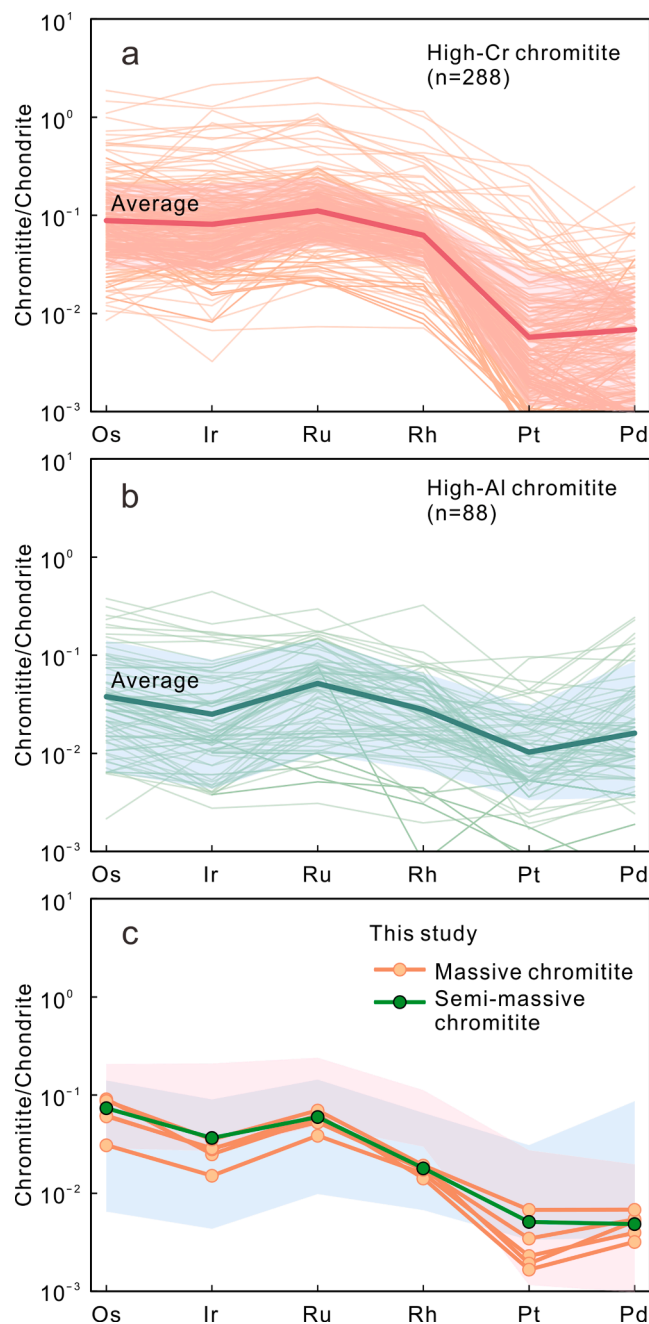
Fig. 12. Chondrite-normalized (Anders and Grevesse, 1989) PGE patterns of the (**a**) high-Cr chromitite, (**b**) high-Al chromitite, and (**c**) Moa-Baracoa chromitite. Colored fields span 10th and 90th percentiles of PGE data. Data sources are same as in Fig. 11.

Miura, 2016; Arai and Yurimoto, 1994;Irvine, 1977; González-Jiménez et al., 2011; Zhou et al., 1994, 1996, 2014). In the Moa-Baracoa high-Al chromitites, occurrence of the PGM and BMS combined with variable Os isotopic composition (Gervilla et al., 2005) suggest mixing/mingling of different magmas. Moreover, the common occurrence of recycled crustal zircons (Proenza et al., 2018) implies that subducted crustal materials may contribute to the formation of the Moa-Baracoa chromitites. The addition of crustal materials can significantly increase the SiO_2 content, which would effectively lower the solubility of Cr in the melt and trigger Cr-spinel precipitation (Bédard and Hébert, 1998; Zhou et al., 2014).

The semi-massive chromitites are free of HP/HT microstructures, and the Cr-spinels are small in size (<3 mm). This suggests that the Cr-spinel of the semi-massive chromitites rapidly crystallized from the

parental magma and were not evidently modified by post-magmatic processes. In contrast, microstructural evidence indicates that the massive chromitites experienced more complex petrogenetic processes. Large grain sizes (3–6 mm), intense crystal-plastic deformation, abundant exsolved needles of clinopyroxene, and clear overgrowth in some Cr-spinel grains of the massive chromitites suggests that they probably crystallized and/or recrystallized under HP/HT conditions for a long period of time. Moreover, olivine inclusions in the Cr-spinels of the massive chromitites have certainly higher contents of Fo and NiO than those of the semi-massive chromitites (Fig. 5a), which indicates Mg and Ni redistribution into olivine during a sufficiently long annealing time in the massive chromitites (Miura et al., 2012). Typical UHP minerals of ophiolitic chromitites, such as diamond and coesite, are absent in the Moa-Baracoa chromitites. This may reflect that the Moa-Baracoa chromitites are intermediate (e.g., Miura et al., 2012; González-Jiménez et al., 2017) between typical LP and UHP chromitites.

HP chromitites are believed to have either crystallized directly in the deep mantle (Miura et al., 2012; Yang et al., 2015, 2021), or initially formed in the shallow mantle and then recycled into the deep mantle before being emplaced in the oceanic lithosphere (Arai, 2013; González-Jiménez et al., 2017; Xiong et al., 2017a). The massive chromitites of this study show both high- and low-pressure signatures, suggesting that some Cr-spinel grains crystallized in a relatively deep mantle. These HP Cr-spinels could have migrated with the upwelling parental magma, deposited with the LP Cr-spinels in the shallow mantle, and formed the massive chromitites (Fig. 16).

6.4. Geodynamic environment of the Ti-poor high-Al chromitites

Ophiolite occurs in various tectonic settings and is an important archive of oceanic crust development and plate tectonic evolution (Dilek and Furnes, 2011; Furnes et al., 2020; Wu et al., 2021). Podiform chromite deposits are exclusively hosted in ophiolitic complexes. Therefore, studying the petrogenesis of podiform chromitite is not only critical for exploration of chromite deposits, but is also important for understanding the origin and tectonic evolution of the host ophiolites (Ahmed et al., 2020; Arai, 2013; Cai et al., 2021; Farré-de-Pablo et al., 2020; González-Jiménez et al., 2017; Lian et al., 2019; Nayak et al., 2021; Rui et al., 2019; Uysal et al., 2009; Xiong et al., 2017a). Generally, high-Cr chromitites are known to form in forearc basins above a supra-subduction zone (Nayak et al., 2021; Uysal et al., 2009; Zhou et al., 1996), while high-Al chromitites form in MOR (Arai and Miura, 2015), back-arc basin (González-Jiménez et al., 2011; Zhu and Zhu, 2020), and nascent forearc during subduction initiation (Lian et al., 2019; Rollinson and Adetunji, 2013; Xiong et al., 2017a; Wu et al., 2019; Zhang et al., 2020).

The Moa-Baracoa high-Al chromitites are characterized by low TiO_2 content. A few occurrences of such Ti-poor high-Al chromitites have been reported, such as the Zambales ophiolite in Philippines (TiO_2 = 0.05–0.22 wt%, Zhang et al., 2020) and the Dongbo ophiolite in Tibet (TiO_2 <0.15 wt%, Xiong et al., 2017b). Coincidently, these Ti-poor high-Al chromitites coexist with high-Cr chromitites and are interpreted to have formed during subduction initiation (Zhang et al., 2020) or transitional tectonic regime from the MOR to the supra-subduction zone (Xiong et al., 2017b).

Silicate inclusion, mineral chemistry, and whole-rock PGE behavior collectively suggest that the Ti-poor high-Al chromitites from the MBOM originated from a previously depleted hydrous mantle source with contamination by subducted sediments. This is consistent with the mantle wedge environment that occurs above a subducting slab. The host harzburgite of these high-Al chromitites underwent a high degree (>25%) of partial melting and are highly refractory in nature (Marchesi et al., 2006; Rui et al., 2021). The mineral chemistry of secondary clinopyroxene and BMS, combined with C-type olivine fabric, suggests that the harzburgite originated from a nascent forearc mantle that was modified by interaction with forearc basaltic melt during subduction
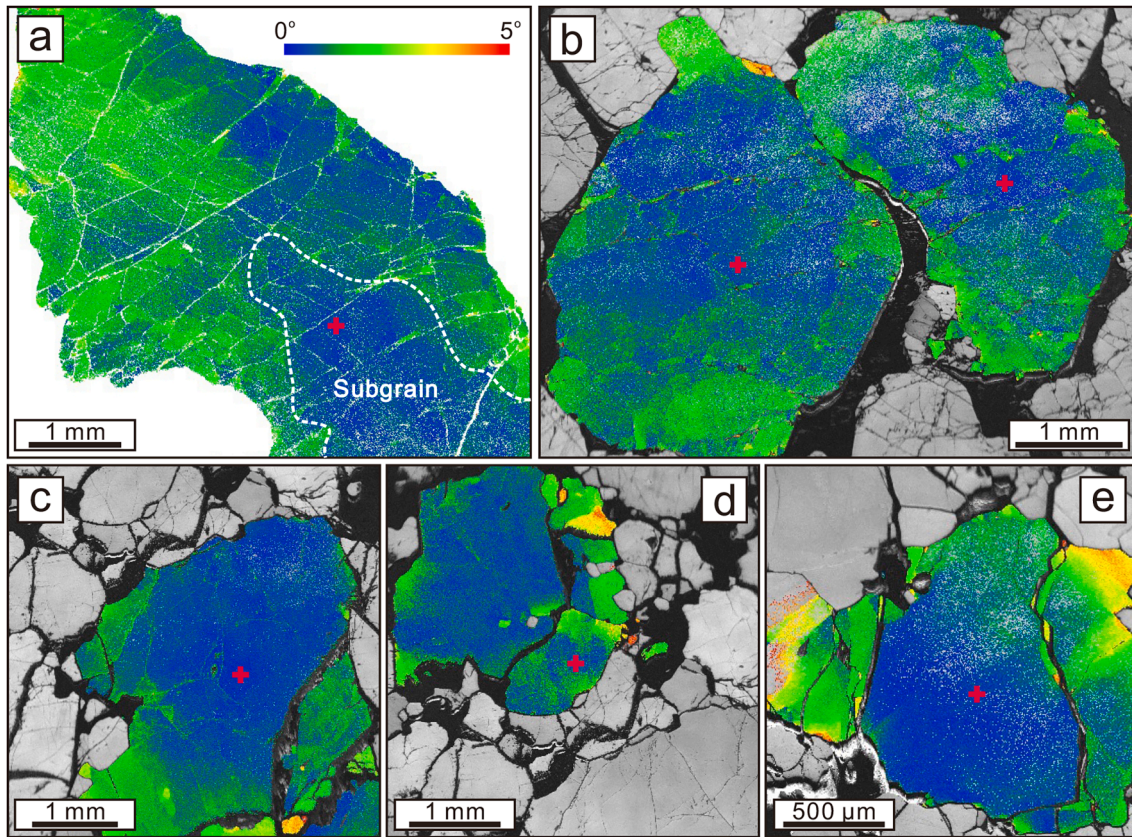
Fig. 13. EBSD misorientation mapping of representative Cr-spinel grains in the massive (**a**–**b**) and semi-massive (**c**–**e**) chromitites of the MBOM.
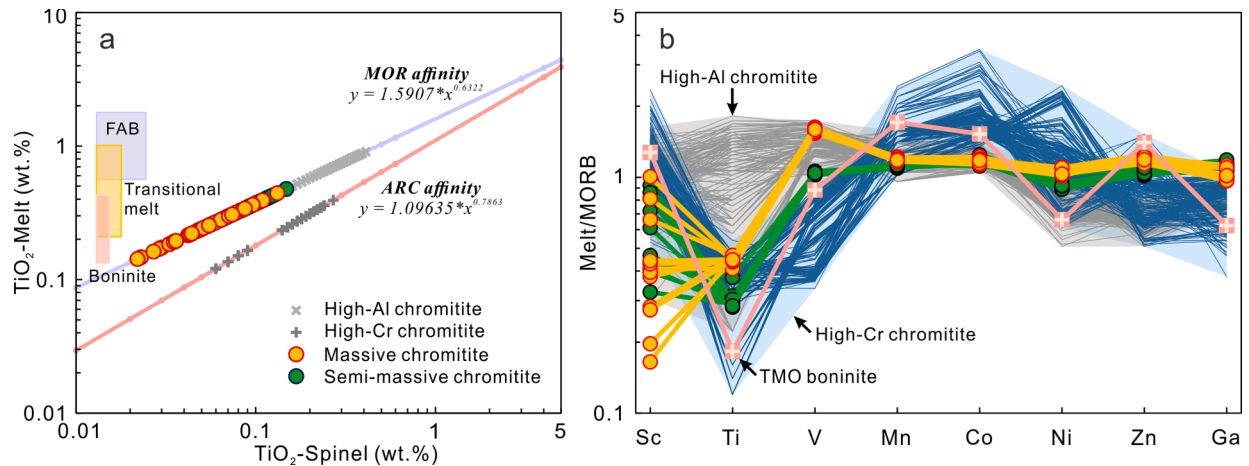

Fig. 14. Calculated parental magma compositions of the Moa-Baracoa chromitites. The empirical formulas are from Rollinson (2008); High-Cr and -Al chromitite data are from Zhou et al. (2014); TMO boninite and MORB data are from Pagé and Barnes (2009).

initiation (Rui et al., 2021). Furthermore, a suit of gabbroic rocks in the MBOM records the onset of subduction of the proto-Caribbean beneath the Caribbean plate (Rui et al., 2022b). Approximately 137–122 Ma gabbroic rocks crystallized from forearc basaltic or subduction-related magma indicate that subduction initiated in the Early Cretaceous (Rojas-Agramonte et al., 2016; Rui et al., 2022b). Combining the origin of the harzburgite and gabbroic rocks, we propose that the Ti-poor high-Al chromitites from the MBOM formed in a nascent forearc mantle during subduction initiation (Fig. 16).

7. Conclusion

Ti-poor high-Al chromitites in the MBOM occur as massive and semi-massive textures in dunite envelopes within host harzburgite. In the massive samples, Cr-spinel grains exhibit both HP (e.g., abundant exsolved needles of clinopyroxene, strong crystal-plastic deformation) and LP characteristics (inclusions of amphibole and phlogopite). Parental magma of the chromitite was estimated to be hydrous with very low TiO_2 and high oxygen fugacity, reflecting a depleted and hydrous mantle source. Mixing/mingling of different magmas and the addition of subducted crustal materials probably triggered the precipitation of Cr-spinel. All these features imply that some Cr-spinel grains crystallized
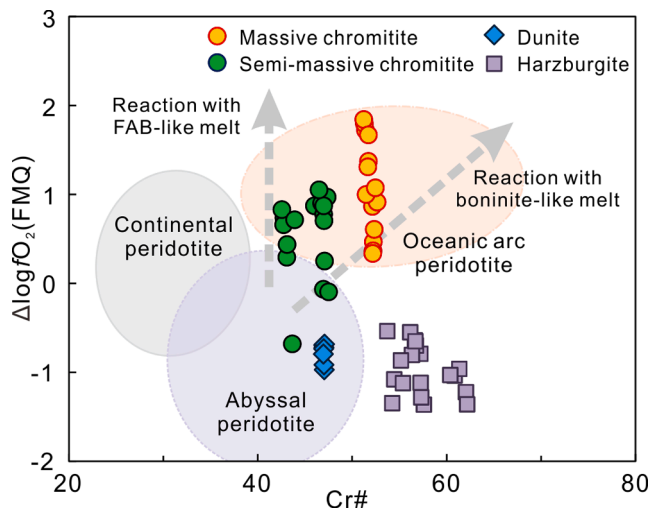
Fig. 15. Plots of $\Delta \log f O_2$(FMQ) vs. Cr# (spinel) for the peridotite and chromitites of the MBOM. The tectonic discrimination fields in are from Parkinson and Pearce (1998).
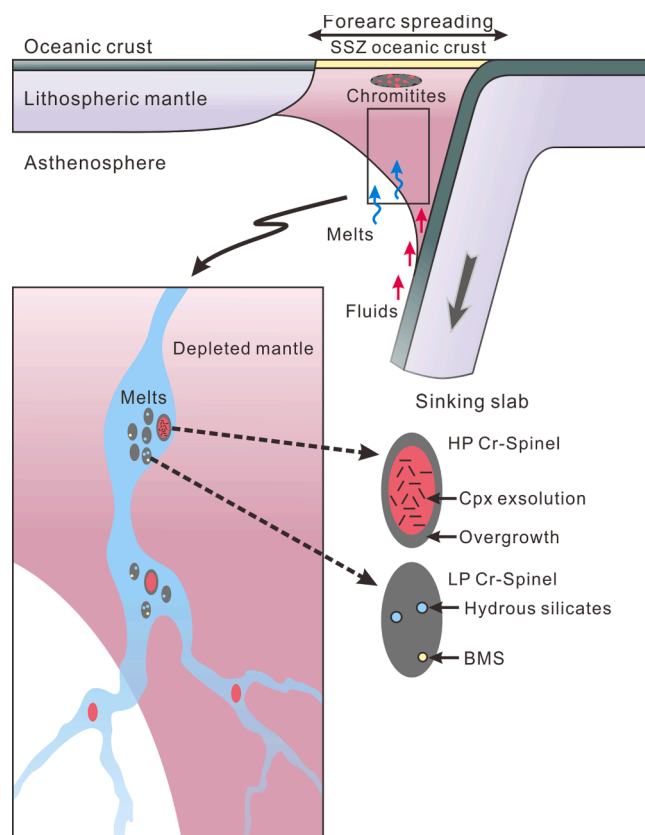
Fig. 16. Schematic cartoons (not to scale) showing the formation of high-Al chromitites in the MBOM.

in a relatively deep mantle, traveled upward with the parental melt, and deposited in the shallow mantle. The formation of Ti-poor high-Al chromitites, coupled with the origin of harzburgites and gabbros in the massif, indicates that the Moa-Baracoa chromitites were generated beneath a forearc basin during subduction initiation.

Declaration of Competing Interest

The authors declare that they have no known competing financial

interests or personal relationships that could have appeared to influence the work reported in this paper.

Appendix A. Supplementary data

Supplementary data to this article can be found online at https://doi.org/10.1016/j.oregeorev.2022.104847.

References

Ahmed, A., Arai, S., 2002. Unexpectedly high-PGE chromitite from the deeper mantle section of the northern Oman ophiolite and its tectonic implications. Contrib. Miner. Petrol. 143 (3), 263–278.

Ahmed, I.N., Kettanah, Y.A., Ismail, S.A., 2020. Genesis and tectonic setting of high-Cr podiform chromitites of the Rayat ophiolite in the Zagros Suture Zone, northeastern Iraq. Ore Geol. Rev. 123, 103583.

Akmaz, R.M., Uysal, I., Saka, S., 2014. Compositional variations of chromite and solid inclusions in ophiolitic chromitites from the southeastern Turkey: implications for chromitite genesis. Ore Geol. Rev. 58, 208–224.

Anders, E., Grevesse, N., 1989. Abundances of the elements: Meteoritic and solar. Geochim. Cosmochim. Acta 53 (1), 197–214.

Arai, S., 2013. Conversion of low-pressure chromitites to ultrahigh-pressure chromitites by deep recycling: a good inference. Earth Planet. Sci. Lett. 379, 81–87.

Arai, S., Ahmed, A.H., 2018. Secular change of chromite concentration processes from the Archean to the Phanerozoic. In: Processes and Ore Deposits of Ultramafic-Mafic Magmas through Space and Time. Elsevier, pp. 139–157.

Arai, S., Miura, M., 2015. Podiform chromitites do form beneath mid-ocean ridges. Lithos 232, 143–149.

Arai, S., Miura, M., 2016. Formation and modification of chromitites in the mantle. Lithos 264, 277–295.

Arai, S., Yurimoto, H., 1994. Podiform chromitites of the Tari-Misaka ultramafic complex, southwestern Japan, as mantle-melt interaction products. Econ. Geol. 89, 1279–1288.

Augé, T., 1987. Chromite deposits in the northern Oman ophiolite: mineralogical constraints. Mineral. Deposita 22, 1–10.

Ballhaus, C., Berry, R.F., Green, D.H., 1991. High pressure experimental calibration of the olivine-orthopyroxene-spinel oxygen geobarometer: implications for the oxidation state of the upper mantle. Contrib. Miner. Petrol. 107 (1), 27–40.

Barnes, S.-J., Naldrett, A.J., Gorton, M.P., 1985. The origin of the fractionation of platinum group elements in terrestrial magmas. Chem. Geol. 53 (3-4), 303–323.

Bédard, J.H., Hébert, R., 1998. Formation of chromitites by assimilation of crustal pyroxenites and gabbros into peridotitic intrusions: North Arm Mountain massif, Bay of Islands ophiolite, Newfoundland, Canada. J. Geophys. Res.: Solid Earth 103, 5165–5184.

Birner, S.K., Warren, J., Cottrell, E., Davis, F.A., Kelley, K.A., Falloon, T.J., 2017. Forearc peridotites from Tonga record heterogeneous oxidation of the mantle following subduction initiation. J. Petrol. 58, 1–25.

Brunelli, D., Seyler, M., Cipriani, A., Ottolini, L., Bonatti, E., 2006. Discontinuous melt extraction and weak refertilization of mantle peridotites at the Vema lithospheric section (Mid-Atlantic Ridge). J. Petrol. 47, 745–771.

Bussolesi, M., Grieco, G., Tzamos, E., 2019. Olivine-spinel diffusivity patterns in chromitites and dunites from the Finero phlogopite-peridotite (Ivrea-Verbano Zone, Southern Alps): Implications for the thermal history of the massif. Minerals 9, 75. https://doi.org/10.3390/min9020075.

Cai, P., Chen, X., Majka, J., Klonowska, I., Jeanneret, P., Xu, R., Zheng, Y., 2021. Two stages of crust-mantle interaction during oceanic subduction to continental collision: Insights from mafic-ultramafic complexes in the North Qaidam orogen. Gondwana Res. 89, 247–264.

Chen, M., Shu, J., Mao, H.-K., Xie, X., Hemley, R.J., 2003. Natural occurrence and synthesis of two new postspinel polymorphs of chromite. P. Natl. Acad. Sci. 100 (25), 14651–14654.

Chen, T., Jin, Z., Zhang, J., Wang, L., 2019. Calcium amphibole exsolution lamellae in chromite from the Semail ophiolite: Evidence for a high-pressure origin. Lithos 334–335, 273–280.

Chen, C., Wang, C.Y., Tan, W., Yao, Z.S., 2021. Origin of chromite nodules in podiform chromitite from the Kızıldğ ophiolite, southern Turkey. Ore Geol. Rev. 139, 104443.

Dick, H.J.B., Bullen, T., 1984. Chromian spinel as a petrogenetic indicator in abyssal and alpine-type peridotites and spatially associated lavas. Contrib. Miner. Petrol. 86 (1), 54–76.

Dilek, Y., Furnes, H., 2011. Ophiolite genesis and global tectonics: Geochemical and tectonic fingerprinting of ancient oceanic lithosphere. Geol. Soc. Am. Bull. 123 (3-4), 387–411.

Dubois-Côté, V., Hébert, R., Dupuis, C., Wang, C.S., Li, Y.L., Dostal, J., 2005. Petrological and geochemical evidence for the origin of the Yarlung Zangbo ophiolites, southern Tibet. Chem. Geol. 214 (3-4), 265–286.

Economou-Eliopoulos, M., Tsoupas, G., Skounakis, V., 2019. Occurrence of graphite-like carbon in podiform chromitites of Greece and its genetic significance. Minerals 9, 152. https://doi.org/10.3390/min9030152.

Farré-de-Pablo, J., Proenza, J.A., González-Jiménez, J.M., Aiglsperger, T., Garcia-Casco, A., Escuder-Viruete, J., Colás, V., Longo, F., 2020. Ophiolite hosted chromitite formed by supra-subduction zone peridotite – plume interaction. Geosci. Front. 11 (6), 2083–2102.

Frei, R., Gervilla, F., Meibom, A., Proenza, J.A., Garrido, C.J., 2006. Os isotope heterogeneity of the upper mantle: evidence from the Mayarí-Baracoa ophiolite belt in eastern Cuba. Earth Planet. Sci. Lett. 241 (3-4), 466–476.

Furnes, H., Dilek, Y., Zhao, G., Safonova, I., Santosh, M., 2020. Geochemical characterization of ophiolites in the Alpine-Himalayan Orogenic Belt: Magmatically and tectonically diverse evolution of the Mesozoic Neotethyan oceanic crust. Earth-Sci. Rev. 208, 103258.

Garuti, G., Fershtater, G., Bea, F., Montero, P., Pushkarev, E.V., Zaccarini, F., 1997. Platinum-group elements as petrological indicators in mafic-ultramafic complexes of central and southern Urals: preliminary results. Tectonophysics 276, 181–194.

Garuti, G., Zaccarini, F., Economou-Eliopoulos, M., 1999. Paragenesis and composition of laurite from chromitites of Othrys (Greece): implications for Os-Ru fractionation in ophiolitic upper mantle of the Balkan peninsula. Mineral. Deposita 34 (3), 312–319.

Gervilla, F., Proenza, J.A., Frei, R., Gonzalez-Jimenez, J.M., Garrido, C.J., Melgarejo, J. C., Meibom, A., Diaz-Martinez, R., Lavaut, W., 2005. Distribution of platinum-group elements and Os isotopes in chromite ores from Mayari-Baracoa Ophiolite Belt (eastern Cuba). Contrib. Miner. Petrol. 150, 589–607.

González-Jiménez, J.M., Camprubí, A., Colás, V., Griffin, W.L., Proenza, J.A., O'Reilly, S. Y., Centeno-García, E., García-Casco, A., Belousova, E., Talavera, C., Farré-de-Pablo, J., Satsukawa, T., 2017. The recycling of chromitites in ophiolites from southwestern North America. Lithos 294–295, 53–72.

González-Jiménez, J.M., Griffin, W.L., Proenza, J.A., Gervilla, F., O'Reilly, S.Y., Akbulut, M., Pearson, N.J., Arai, S., 2014. Chromitites in ophiolites: how, where, when, why? Part II. The crystallisation of chromitites. *Lithos* 189, 140–158.

González-Jiménez, J.M., Proenza, J.A., Gervilla, F., Melgarejo, J.C., Blanco-Moreno, J.A., Ruiz-Sánchez, R., Griffin, W.L., 2011. High-Cr and high-Al chromitites from the Sagua de Tánamo district, Mayarí-Cristal ophiolitic massif (eastern Cuba): Constraints on their origin from mineralogy and geochemistry of chromian spinel and platinum-group elements. Lithos 125 (1-2), 101–121.

González-Jiménez, J.M., Proenza, J.A., Pastor-Oliete, M., Saunders, E., Aiglsperger, T., Pujol-Solà, N., Melgarejo, J.C., Gervilla, F., Garcia-Casco, A., 2020. Precious metals in magmatic Fe-Ni-Cu sulfides from the Potosí chromitite deposit, eastern Cuba. Ore Geol. Rev. 118, 103339.

Grieco, G., Bussolesi, M., Eslami, A., Gentile, A., Cavallo, A., Lian, D., Yang, J., Ghaseminejad, J., 2020. Differential platinum group elements (PGE) re-mobilization at low fS2 in Abdasht and Soghan mafic-ultramafic complexes (Southern Iran). Lithos 366–367, 105523.

Grieco, G., Diella, V., Chaplygina, N.L., Savelieva, G.N., 2007. Platinum group elements zoning and mineralogy of chromitites from the cumulate sequence of the Nurali massif (Southern Urals, Russia). Ore Geol. Rev. 30 (3-4), 257–276.

Griffin, W.L., Afonso, J.C., Belousova, E.A., Gain, S.E., Gong, X.-H., González-Jiménez, J. M., Howell, D., Huang, J.-X., McGowan, N., Pearson, N.J., Satsukawa, T., Shi, R., Williams, P., Xiong, Q., Yang, J.-S., Zhang, M., O'Reilly, S.Y., 2016. Mantle recycling: transition-zone metamorphism of Tibetan ophiolitic peridotites and its tectonic implications. J. Petrol. 57 (4), 655–684.

Günay, K., Çolakoğlu, A.R., 2016. Spinel compositions of mantle-hosted chromitite from the Eastern Anatolian ophiolite body, Turkey: implications for deep and shallow magmatic processes. Ore Geol. Rev. 73, 29–41.

Habtoor, A.M., Ahmed, A.H., Akizawa, N., Harbi, H., Arai, S., 2017. Chemical homogeneity of high-Cr chromitites as indicator for widespread invasion of boninitic melt in mantle peridotite of Bir Tuluha ophiolite, Northern Arabian Shield, Saudi Arabia. Ore Geol. Rev. 90, 243–259.

Hamlyn, P.R., Keays, R.R., 1986. Sulphur saturation and second stage melts; application to the Bushveld Pt metal deposits. Econ. Geol. 81, 1431–1445.

Irvine, T.N., 1977. Origin of chromite layers in the Muskox intrusion and other intrusions: a new interpretation. Geology 5, 273–277.

Ishii, T., Robinson, P.T., Maekawa, H., Fiske, R., 1992. Petrological studies of peridotites from diapiric serpentinite seamounts in the Izu–Ogasawara–Mariana forearc, Leg 125. In: Fryer, P., Pearce, J.A., Stokking, L.B. (Eds.), Proceedings of the Ocean Drilling Program Scientific Results 125. Ocean Drilling Program, College Station, TX, pp. 445–486.

Ismail, S.A., Kettanah, Y.A., Chalabi, S.N., Ahmed, A.H., Arai, S., 2014. Petrogenesis and PGE distribution in the Al- and Cr-rich chromitites of the Qalander ophiolite, northeastern Iraq: implications for the tectonic environment of the Iraqi Zagros Suture Zone. Lithos 202–203, 21–36.

Ismail, S.A., Mirza, T.M., Carr, P.F., 2010. Platinum-group elements geochemistry in podiform chromitites and associated peridotites of the Mawat ophiolite, northeastern Iraq. J. Asian Earth Sci. 37 (1), 31–41.

Iturralde-Vinent, M.A., Díaz-Otero, C., Rodríguez-Vega, A., Díaz-Martínez, R., 2006. Tectonic implications of paleontologic dating of Cretaceouse-Danian sections of Eastern Cuba. Geol. Acta 4, 89–102.

Kamenetsky, V.S., Crawford, A.J., Meffre, S., 2001. Factors controlling chemistry of magmatic spinel: an empirical study of associated olivine, Cr-spinel and melt inclusions from primitive rocks. J. Petrol. 42 (4), 655–671.

Lázaro, C., Blanco-Quintero, I.F., Proenza, J.A., Rojas-Agramonte, Y., Neubauer, F., Núñez-Cambra, K., Garcia-Casco, A., 2016. Petrogenesis and $^{40}Ar/^{39}Ar$ dating of proto-forearc crust in the early cretaceous Caribbean arc: the La Tinta mélange (eastern Cuba) and its easterly correlation in Hispaniola. Int. Geol. Rev. 58 (8), 1020–1040.

Lian, D., Yang, J., Dilek, Y., Rocholl, A., 2019. Mineralogy and geochemistry of peridotites and chromitites in the Aladag Ophiolite (southern Turkey): Melt evolution of the cretaceous Neotethyan mantle. J. Geol. Soc. 176 (5), 958–974.

Lian, D., Yang, J., Dilek, Y., Wiedenbeck, M., Wu, W., Rocholl, A., 2020. Precambrian zircons in chromitites of the Cretaceous Aladag Ophiolite (Turkey) indicate deep crustal recycling in oceanic mantle. Precambrian Res. 350, 105838.

Lian, D., Yang, J., Xiong, F., Liu, F., Wang, Y., 2015. Platinum-group element characteristics of the peridotite and podiform chromitite from Dajiweng ophiolite of the western segment of Yarlung- Zangbo suture zone, Tibet. Geol. China 42, 525–546.

Liu, Y., Hu, Z., Gao, S., Günther, D., Xu, J., Gao, C., Chen, H., 2008. In situ analysis of major and trace elements of anhydrous minerals by LA-ICP-MS without applying an internal standard. Chem. Geol. 257 (1-2), 34–43.

Malitch, K.N., Junk, S.A., Thalhammer, O.A.R., Melcher, F., Knauf, V.V., Pernika, E., Stumpfl, E.F., 2003. Laurite and ruarsite from podiform chromitite at Kraubath and Hochgrossen, Austria: new insights from osmium isotopes. Can. Mineral. 41, 331–352.

Marchesi, C., Garrido, C.J., Bosch, D., Proenza, J.A., Gervilla, F., Moñié, P., Rodríguez-Vega, A., 2007. Geochemistry of cretaceous magmatism in eastern Cuba: Recycling of north American continental sediments and implications for subduction polarity in the Greater Antilles Paleo-arc. J. Petrol. 48, 1813–1840.

Marchesi, C., Garrido, C.J., Godard, M., Proenza, J.A., Gervilla, F., Blanco-Moreno, J., 2006. Petrogenesis of highly depleted peridotites and gabbroic rocks from the Mayarí-Baracoa Ophiolitic Belt (eastern Cuba). Contrib. Miner. Petrol. 151 (6), 717–736.

Marchesi, C., González-Jiménez, J.M., Gervilla, F., Garrido, C.J., Griffin, W.L., O'Reilly, S.Y., Proenza, J.A., Pearson, N.J., 2011. In situ Re–Os isotopic analysis of platinum-group minerals from the Mayarí-Cristal ophiolitic massif (Mayarí–Baracoa Ophiolitic Belt, eastern Cuba): implications for the origin of Os-isotope heterogeneities in podiform chromitites. Contrib. Miner. Petrol. 161 (6), 977–990.

Matveev, S., Ballhaus, C., 2002. Role of water in the origin of podiform chromitite deposits. Earth Planet. Sci. Lett. 203 (1), 235–243.

Maurel, C., Maurel, P., 1982. Experimental study of the solubility of chromium in mafic silicate baths and its partitioning between liquid and coexisting minerals: conditions of existence of chromian magnesiochromite. Bull. Mineral. 105, 640–647.

Melcher, F., Grum, W., Simon, G., Thalhammer, T.V., Stumpfl, E.F., 1997. Petrogenesis of the ophiolitic giant chrome deposits of Kempirsai, Kazakhstan: a study of solid and fluid inclusions in chromite. J. Petrol. 38 (10), 1419–1458.

Melcher, F., Grum, W., Thalhammer, T.V., Thalhammer, O.A.R., 1999. The giant chromite deposits at Kempirsai, Urals; constraints from trace element (PGE, REE) and isotope data. Mineral. Deposita 23 (3), 250–272.

Merlini, A., Grieco, G., Diella, V., 2009. Ferritchromite and chromian-chlorite formation in mélange-hosted Kalkan chromitite (Southern Urals, Russia). Am. Mineral. 94, 1459–1467.

Miura, M., Arai, S., Ahmed, A.H., Mizukami, T., Okuno, M., Yamamoto, S., 2012. Podiform chromitite classification revisited: A comparison of discordant and concordant chromitite pods from Wadi Hilti, northern Oman ophiolite. J. Asian Earth Sci. 59, 52–61.

Naldrett, A.J., von Gruenewaldt, G., 1989. Association of platinum-group elements with chromitite in layered intrusions and ophiolite complexes. Econ. Geol. 84, 180–187.

Nayak, R., Pal, D., Chinnasamy, S.S., 2021. High-Cr chromitites of the Nidar Ophiolite Complex, northern India: Petrogenesis and tectonic implications. Ore Geol. Rev. 129, 103942.

Niida, K., Green, D.H., 1999. Stability and chemical composition of pargasitic amphibole in MORB pyrolite under upper mantle conditions. Contrib. Miner. Petrol. 135, 18–40.

Pagé, P., Barnes, S.J., 2009. Using trace elements in chromite to constrain the origin of podiform chromitites in the Thetfod Mines ophiolite, Québec, Canada. Econ. Geol. 104, 997–1018.

Parkinson, I.J., Pearce, J.A., 1998. Peridotites from the Izu-Bonin-Mariana forearc (ODP Leg125): evidence for mantle melting and melt-mantle interaction in a suprasubduction zone setting. J. Petrol. 39 (9), 1577–1618.

Pearce, J.A., Barker, P.F., Edwards, S.J., Parkinson, I.J., Leat, P.T., 2000. Geochemistry and tectonic significance of peridotites from the South Sandwich arc-basin system, South Atlantic. Contrib. Miner. Petrol. 139 (1), 36–53.

Peighambari, S., Uysal, I., Stosch, H.-G., Ahmadipour, H., Heidarian, H., 2016. Genesis and tectonic setting of ophiolitic chromitites from the Dehsheikh ultramafic complex (Kerman, southeastern Iran): Inferences from platinum-group elements and chromite compositions. Ore Geol. Rev. 74, 39–51.

Prichard, H.M., Neary, C.R., Fisher, P.C., O'Hara, M.J., 2008. PGE-rich podiform chromitites in the Al 'Ays Ophiolite Complex, Saudi Arabia: An example of critical mantle melting to extract and concentrate PGE. Econ. Geol. 103 (7), 1507–1529.

Proenza, J.A., Díaz-Martínez, R., Iriondo, A., Marchesi, C., Melgarejo, J.C., Gervilla, F., Garrido, C.J., Rodríguez-Vega, A., Lozano-Santacruz, R., Blanco-Moreno, J.A., 2006.

Primitive island-arc Cretaceous volcanic rocks in eastern Cuba: The Téneme Formation. Geol. Acta 4, 103–121.

Proenza, J., Gervilla, F., Melgarejo, J., Vera, O., Alfonso, P., Fallick, A., 2001. Genesis of sulfide-rich chromite ores by the interaction between chromitite and pegmatitic olivine–norite dikes in the Potosí Mine (Moa-Baracoa ophiolitic massif, eastern Cuba). Mineral. Deposita 36 (7), 658–669.

Proenza, J.A., Gervilla, F., Melgarejo, J.C., Bodinier, J.L., 1999. Al and Cr rich chromitites from the Mayari-Baracoa Ophiolitic Belt, (eastern Cuba): consequence of interaction between volatile-rich melts and peridotite in suprasubduction mantle. Econ. Geol. 94, 547–566.

Proenza, J.A., González-Jiménez, J.M., Garcia-Casco, A., Belousova, E., Griffin, W.L., Talavera, C., Rojas-Agramonte, Y., Aiglsperger, T., Navarro-Ciurana, D., Pujol-Solà, N., Gervilla, F., O'Reilly, S.Y., Jacob, D.E., 2018. Cold plumes trigger contamination of oceanic mantle wedges with continental crust-derived sediments: Evidence from chromite zircon grains of eastern Cuban ophiolites. Geosci. Front. 9 (6), 1921–1936.

Pujol-Solà, N., Garcia-Casco, A., Proenza, J.A., González-Jiménez, J.M., del Campo, A., Colás, V., Canals, À., Sánchez-Navas, A., Roqué-Rossell, J., 2020a. Diamond forms during low pressure serpentinisation of oceanic lithosphere. Geochem. Persp. Let. 15, 19–24.

Pujol-Solà, N., Proenza, J.A., Garcia-Casco, A., González-Jiménez, J.M., Andreazini, A., Melgarejo, J.C., Gervilla, F., 2018. An Alternative Scenario on the Origin of Ultra-HighPressure (UHP) and Super-Reduced (SuR) Minerals inOphiolitic Chromitites: A Case Study from the Mercedita Deposit (Eastern Cuba). Minerals 8, 433. https://doi.org/10.3390/min8100433.

Pujol-Solà, N., Proenza, J.A., Garcia-Casco, A., González-Jiménez, J.M., Román-Alpiste, M.J., Garrido, C.J., Melgarejo, J.C., Gervilla, F., Llovet, X., 2020b. Fe-Ti-Zr metasomatism in the oceanic mantle due to extreme differentiation of tholeiitic melts (Moa-Baracoa ophiolite, Cuba). Lithos 358–359, 105420.

Qiu, T., Yang, J., Milushi, I., Wu, W., Mekshiqi, N., Xiong, F., Zhang, C., Shen, T., 2018. Petrology and PGE abundances of high-Cr and high-Al podiform chromitites and peridotites from the Bulqiza ultramafic massif, eastern Mirdita ophiolite, Albania. Acta Geol. Sin-Engl. 92 (3), 1063–1081.

Robinson, P.T., Trumbull, R.B., Schmitt, A., Yang, J.-S., Li, J.-W., Zhou, M.-F., Erzinger, J., Dare, S., Xiong, F., 2015. The origin and significance of crustal minerals in ophiolitic chromitites and peridotites. Gondwana Res. 27 (2), 486–506.

Rojas-Agramonte, Y., Garcia-Casco, A., Kemp, A., Kröner, A., Proenza, J.A., Lázaro, C., Liu, D., 2016. Recycling and transport of continental material through the mantlewedge above subduction zones: A Caribbean example. Earth Planet. Sc. Lett. 436, 93–107.

Rollinson, H., 2008. The geochemistry of mantle chromitites from the northern part of the Oman ophiolite: inferred parental melt compositions. Contrib. Miner. Petrol. 156 (3), 273–288.

Rollinson, H., Adetunji, J., 2013. Mantle podiform chromitites do not form beneath midocean ridges: a case study from the Moho transition zone of the Oman ophiolite. Lithos 177, 314–327.

Rui, H., Jiao, J., Xia, M., Yang, J., Xia, Z., 2019. Origin of chromitites in the Songshugou peridotite massif, Qinling Orogen (Central China): Mineralogical and geochemical evidence. J. Earth Sci. 30 (3), 476–493.

Rui, H.C., Yang, J.S., Llanes-Castro, A.I., Zheng, J.P., Liu, F., Valdes-Mariño, Y., Wu, W. W., Qiu, T., 2021. Highly refractory harzburgites from the Moa-Baracoa Ophiolitic Massif, Eastern Cuba: Insights into forearc mantle melt-rock interactions. Lithos 404–405, 106427.

Rui, H.C., Yang, J.S., Lian, D.Y., Wu, W.W., Guo, G.L., 2022a. Deep origin of mantle peridotites from the Aladag ophiolite, Turkey: Implication from trace element geochemistry of pyroxenes and mineralogy of ophiolitic chromitites. J. Asian Earth Sci. 228, 105153 https://doi.org/10.1016/j.jseaes.2022.105153.

Rui, H.C., Yang, J.S., Zheng, J.P., Llanes-Castro, A.I., Liu, F., Wu, Y., Wu, W.W., Valdes-Mariño, Y., Masoud, A.E., 2022b. Early Cretaceous subduction initiation of the proto-Caribbean plate: geochronological and geochemical evidence from gabbros of the Moa-Baracoa ophiolitic massif, Eastern Cuba. Lithos 418–419, 106674. https://doi.org/10.1016/j.lithos.2022.106674.

Satsukawa, T., Griffin, W.L., Piazolo, S., O'Reilly, S.Y., 2015. Messengers from the deep: Fossil wadsleyite-chromite microstructures from the Mantle Transition Zone. Sci. Rep. 5, 16484.

Saveliev, D.E., 2021. Chromitites of the Kraka ophiolite (South Urals, Russia): geological, mineralogical and structural features. Miner Deposita 56 (6), 1111–1132.

Sepidbar, F., Khedr, M.Z., Ghorbani, M.R., Palin, R.M., Xiao, Y., 2021. Petrogenesis of arc-related peridotite hosted chromitite deposits in Sikhoran-Soghan mantle section, South Iran: Evidence for proto-forearc spreading to boninitic stages. Ore Geol. Rev. 136, 104256.

Seyler, M., Cannat, M., Mével, C., 2003. Evidence for major-element heterogeneity in the mantle source of abyssal peridotites from the Southwest Indian Ridge (52° to 68°E). Geochem. Geophys. Geosyst. 4 (2), 9101.

Shi, R., Alard, O., Zhi, X., O'Reilly, S.Y., Pearson, N.J., Griffin, W.L., Zhang, M., Chen, X., 2007. Multiple events in the Neo-Tethyan oceanic upper mantle: evidence from Ru-Os-Ir alloys in the Luobusa and Dongqiao ophiolitic podiform chromitites, Tibet. Earth Planet. Sci. Lett. 261 (1-2), 33–48.

Sideridis, A., Zaccarini, F., Koutsovitis, P., Grammatikopoulos, T., Tsikouras, B., Garuti, G., Hatzipanagiotou, K., 2021. Chromitites from the Vavdos ophiolite (Chalkidiki, Greece): Petrogenesis and geotectonic settings; constrains from spinel, olivine composition, PGE mineralogy and geochemistry. Ore Geol. Rev. 137, 104289.

Silk, M.H., 1988. World chromite resources and ferrichromite production. MINTEK, Special Publication no 1. Council for Mineral Technology, Randburg.

Su, B.X., Robinson, P.T., Chen, C., Xiao, Y., Melcher, F., Bai, Y., Gu, X.Y., Uysal, I., Lenaz, D., 2020. The occurrence, origin, and fate of water in chromitites in ophiolites. Am. Mineral. 105, 894–903.

Su, B.X., Zhou, M.F., Robinson, P.T., 2016. Extremely large fractionation of Li isotopes in a chromitite-bearing mantle sequence. Sci. Rep. 6, 22370.

Sun, C., Liang, Y., 2012. Distribution of REE between clinopyroxene and basaltic melt along a mantle adiabat: Effects of major element composition, water, and temperature. Contrib. Miner. Petrol. 163 (5), 807–823.

Sun, S.-s., McDonough, W.F., 1989. Chemical and isotopic systematics of oceanic basalts: implications for mantle composition and processes. Geol. Soc. Spec. Publ. 42 (1), 313–345.

Takahashi, E., Uto, K., Schilling, J.-G., 1987. Primary magma compositions and Mg/Fe ratios of their mantle residues along Mid Atlantic Ridge 29°N to 73°N. Techn. Rep. Inst. Stud. Earth`s Inter. Series A 9, 1–14.

Ullah, Z., Shah, M.T., Siddiqui, R.H., Lian, D.-Y., Khan, A., 2020a. Petrochemistry of high Cr and high-Al chromitites occurrences of Dargai complex along Indus suture zone, northern Pakistan. Episodes 43 (2), 689–709.

Ullah, Z., Li, J.W., Robinson, P.T., Wu, W.W., Khan, A., Dac, N.X., Adam, M.M.A., 2020b. Mineralogy and geochemistry of peridotites and chromitites in the Jijal complex ophiolite along the Main Mantle Thrust (MMT or Indus Suture Zone) North Pakistan. Lithos 366–367, 105566.

Uysal, I., Akmaz, R.M., Kapsiotis, A., Demir, Y., Saka, S., Avcı, E., Müller, D., 2015. Genesis and geodynamic significance of chromitites from the Orhaneli and Harmancık ophiolites (Bursa, NW Turkey) as evidenced by mineralogical and compositional data. Ore Geol. Rev. 65, 26–41.

Uysal, I., Akmaz, R.M., Saka, S., Kapsiotis, A., 2016. Coexistence of compositionally heterogeneous chromitites in the Antalya-Isparta ophiolitic suite, SW Turkey: a record of sequential magmatic processes in the sub-arc lithospheric mantle. Lithos 248–251, 160–174.

Uysal, I., Kapsiotis, A., Akmaz, R.M., Saka, S., Seitz, H.M., 2018. The Guleman ophiolitic chromitites (SE Turkey) and their link to a compositionally evolving mantle source during subduction initiation. Ore Geol. Rev. 93, 98–113.

Uysal, İ., Tarkian, M., Sadiklar, M.B., Zaccarini, F., Meisel, T., Garuti, G., Heidrich, S., 2009. Petrology of Al- and Cr-rich ophiolitic chromitites from the Muğla, SW, Turkey: implications from composition of chromite, solid inclusions of platinum-group mineral, silicate, and base-metal mineral, and Os-isotope geochemistry. Contrib. Miner. Petrol. 158 (5), 659–674.

Wu, Y., Xu, M., Jin, Z., Fei, Y., Robinson, P.T., 2016. Experimental constraints on the formation of the Tibetan podiform chromitites. Lithos 245, 109–117.

Wu, W., Yang, J., Dilek, Y., Milushi, I., Lian, D., 2019. Multiple episodes of melting, depletion, and enrichment of the Tethyan mantle: Petrogenesis of the peridotites and chromitites in the Jurassic Skenderbeu massif, Mirdita ophiolite, Albania. Lithosphere 10, 54–78.

Wu, W., Yang, J., Lian, D., Rui, H., 2021. New concepts in ophiolites, oceanic lithosphere and podiform chromites. In: Alderton, D., Elias, S.A. (Eds.), Encyclopedia of Geology, second ed. Academic Press, pp. 968–993.

Xiong, F., Yang, J., Robinson, P.T., Xu, X., Liu, Z., Li, Y., Li, J., Chen, S., 2015. Origin of podiform chromitite, a new model based on the Luobusa ophiolite, Tibet. Gondwana Res. 27 (2), 525–542.

Xiong, F., Yang, J., Robinson, P.T., Xu, X., Liu, Z., Zhou, W., Feng, G., Xu, J., Li, J., Niu, X., 2017a. High-Al and high-Cr podiform chromitites from the western Yarlung-Zangbo suture zone, Tibet: Implications from mineralogy and geochemistry of chromian spinel, and platinum-group elements. Ore Geol. Rev. 80, 1020–1041.

Xiong, F., Yang, J., Xu, X., Kapsiotis, A., Hao, X., Liu, Z., 2018. Compositional and isotopic heterogeneities in the Neo-Tethyan upper mantle recorded by coexisting Al-rich and Cr-rich chromitites in the Purang peridotite massif, SW Tibet (China). J. Asian Earth Sci. 159, 109–129.

Xiong, F., Zoheir, B., Robinson, P.T., Yang, J., Xu, X., Meng, F., 2020. Genesis of the Ray-Iz chromitite, Polar Urals: Inferences to mantle conditions and recycling processes. Lithos 374–375, 105699.

Xiong, F., Zoheir, B., Wirth, R., Milushi, I., Qiu, T., Yang, J., 2021. Mineralogical and isotopic peculiarities of high-Cr chromitites: Implications for a mantle convection genesis of the Bulqiza ophiolite. Lithos 398–399, 106305.

Xiong, Q., Henry, H., Griffin, W.L., Zheng, J., Satsukawa, T., Pearson, N.J., O'Reilly, S.Y., 2017b. High- and low-Cr chromitite and dunite in a Tibetan ophiolite: Evolution from mature subduction system to incipient forearc in the Neo-Tethyan Ocean. Contrib. Miner. Petrol. 172, 45. https://doi.org/10.1007/s00410-017-1364-y.

Yamamoto, S., Komiya, T., Hirose, K., Maruyama, S., 2009. Coesite and clinopyroxene exsolution lamellae in chromites: in-situ ultrahigh-pressure evidence from podiform chromitites in the Luobusa ophiolite, southern Tibet. Lithos 109 (3-4), 314–322.

Yang, J., Meng, F., Xu, X., Robinson, P.T., Dilek, Y., Makeyev, A.B., Wirth, R., Wiedenbeck, M., Cliff, J., 2015. Diamonds, native elements and metal alloys from chromitites of the Ray-Iz ophiolite of the Polar Urals. Gondwana Res. 27 (2), 459–485.

Yang, J.S., Dobrzhinetskaya, L., Bai, W.J., Fang, Q.S., Robinson, P.T., Zhang, J., Green, H. W., 2007. Diamond-and coesite-bearing chromitites from the Luobusa ophiolite. Tibet. *Geology* 35, 875–878.

Yang, J.S., Wu, W.W., Lian, D.Y., Rui, H.C., 2021. Peridotites, chromitites and diamonds in ophiolites. Nat. Rev. Earth Environ. 2, 198–212. https://doi.org/10.1038/s43017-020-00138-4.

Zhang, Y.F., Jin, Z.M., Griffin, W.L., Wang, C., Wu, Y., 2017a. High-pressure experiments provide insights into the Mantle Transition Zone history of chromitite in Tibetan ophiolites. Earth Planet. Sci. Lett. 463, 151–158.

Zhang, P.F., Zhou, M.F., Su, B.X., Uysal, I., Robinson, P.T., Avcı, E., He, Y.S., 2017b. Iron isotopic fractionation and origin of chromitites in the paleo-Moho transition zone of the Kop ophiolite, NE Turkey. Lithos 268, 65–75.

Zhang, P.F., Zhou, M.F., Yumul Jr., G.P., 2020. Coexistence of high-Al and high-Cr chromite orebodies in the Acoje block of the Zambales ophiolite, Philippines: evidence for subduction initiation. Ore Geol. Rev. 126, 103739.

Zhou, M., Lewis, J., Malpas, J., Munoz-Gomez, N., 2001. The Mayarí-Baracoa paired ophiolite belt, eastern Cuba: Implications for tectonic settings and platinum-group elemental mineralization. Int. Geol. Rev. 43, 494–507.

Zhou, M.F., Robinson, P.T., Bai, W.J., 1994. Formation of podiform chromitites by melt/rock interaction in the upper mantle. Mineral. Deposita 29 (1), 98–101.

Zhou, MEI.-FU., Robinson, P.T., Malpas, JOHN, Li, ZIJIN, 1996. Podiform chromitites in the Luobusa ophiolite (southern Tibet): implications for melt-rock interaction and chromite segregation in the upper mantle. J. Petrol. 37 (1), 3–21.

Zhou, M.F., Robinson, P.T., Su, B.X., Gao, J.F., Li, J.W., Yang, J.S., Malpas, J., 2014. Compositions of chromite, associated minerals, and parental magmas of podiform chromite deposits: the role of slab contamination of asthenospheric melts in supersubduction zone environments. Gondwana Res. 26, 262–283.

Zhou, M.-F., Sun, M., Keays, R.R., Kerrich, R.W., 1998. Controls on platinum-group elemental distributions of podiform chromitites: a case study of high-Cr and high-Al chromitites from Chinese orogenic belts. Geochim. Cosmochim. Acta 62 (4), 677–688.

Zhu, Q., Zhu, Y., 2020. Chromitite genesis based on chrome-spinels and their inclusions in the Sartohay podiform chromitites in west Junggar of northwest China. Ore Geol. Rev. 119, 103401.